THERMAL MANAGEMENT IN HIGH-POWER LASER DIODES BY WAVEGUIDE DESIGN

A THESIS SUBMITTED TO
THE GRADUATE SCHOOL OF ENGINEERING AND SCIENCE
OF BILKENT UNIVERSITY
IN PARTIAL FULFILLMENT OF THE REQUIREMENTS FOR
THE DEGREE OF
MASTER OF SCIENCE
IN
MATERIAL SCIENCE AND NANOTECHNOLOGY

By
Ali Kaan Sünnetçioğlu
August 2023

Thermal Management in High-Power Laser Diodes by Waveguide Design
By Ali Kaan Sünnetçioğlu
August 2023

We certify that we have read this thesis and that in our opinion it is fully adequate, in scope and in quality, as a thesis for the degree of Master of Science.

Abdullah Demir (Advisor)

Alpan Bek

Bülend Ortaç

Approved for the Graduate School of Engineering and Science:

Orhan Arıkan
Director of the Graduate School

ABSTRACT

THERMAL MANAGEMENT IN HIGH-POWER LASER DIODES BY WAVEGUIDE DESIGN

Ali Kaan Sünnetçioğlu
M.S. in Material Science and Nanotechnology
Advisor: Abdullah Demir
August 2023

Semiconductor edge-emitting laser diodes (LDs) are known for their high efficiencies but face challenges in managing self-heating at high operating currents and output powers. The excessive heat density experienced by LDs can lead to critical temperature levels, resulting in catastrophic optical damage (COD) and device failure. Understanding the root cause of COD is crucial for enhancing their reliability and operating output power. This thesis investigates the self-heating mechanism in LDs and introduces novel waveguide designs for thermal management. Initially, we experimentally analyzed LDs with varying waveguide widths to uncover the cause of their failure mechanism. Narrower waveguide LDs achieved higher output power densities but maintained lower internal and facet temperatures. The thermal simulation results showed that narrower waveguide LDs exhibit improved three-dimensional heat dissipation, reducing internal and facet temperatures. The results clarified the fundamental reasons behind the superior reliability of narrower waveguide LDs. Next, we designed and fabricated LDs with two different types of waveguides for their thermal management. The first design introduced a two-section waveguide, which moved the laser section heating away from the facet by positioning a window section near the output facet that is pumped to transparency. This approach reduced facet temperature below the laser internal temperature and eliminated the catastrophic optical mirror damage (COMD) failure. The second design, a distributed waveguide (DWG), increased the lateral heat-dissipation area with passive sections between the laser sections. This method achieved LD cooling by effectively dissipating self-heating and reducing the facet temperature. These findings provide valuable guidance for thermal management to realize LDs with significantly improved reliability and lifetime.

Keywords: Semiconductor laser, diode laser, high power, waveguide design, catastrophoc optical damage (COD).

ÖZET

YÜKSEK GÜÇLÜ LAZER DİYOTLARDA DALGA KILAVUZU TASARIMI İLE ISI YÖNETİMİ

Ali Kaan Sünnetçioğlu
Malzeme Bilim ve Nanoteknoloji, Yüksek Lisans
Tez Danışmanı: Abdullah Demir
Ağustos 2023

Yarıiletken lazer diyotlar (LD'ler) yüksek verimlilikleriyle tanınır ancak performansları yüksek çalışma akımları ve güçlerinde ısıyı yönetme zorluğu nedeniyle tehlikeye girer. LD'lerin yoğun ısı yükleri sıcaklıklarının kritik seviyelere ulaşmasına yol açarak yıkıcı optik hasar (COD) ile cihaz ölümüne yol açabilir. COD'nin kök nedenini anlamak, güvenilirliklerini artırmak ve çalışma çıkış gücünü geliştirmek için büyük önem taşımaktadır. Bu tez çalışması LD'lerin ısınma mekanizmalarını araştırarak ısıl iyileştirme için yeni dalga kılavuzu tasarımları sunmaktadır. Öncelikle, deneyler ve üç boyutlu ısı transferi simülasyon modeli aracılığıyla dalga kılavuzu genişliğinin COD üzerindeki etkisini araştırdık. Bulgularımız, geniş ve dar dalga kılavuzu yapılarına sahip LD'lerin ısı dağılımları arasında belirgin farklar ortaya koydu. Sonrasında, dalga kılavuzunda elektriksel olarak izole edilmiş bölümler kullanan iki farklı türde yüksek güçlü LD tasarladık ve ürettik. İlk tasarımda iki bölümlü dalga kılavuz yapısı üzerine çalıştık. Bu tasarımda çıkış yüzeyine yakın bir bölümün düşük akımda çalışmasıyla saydamlığı sağlanarak lazer bölümünün ısınması lazer çıkış yüzeyinden uzaklaştırıldı. Bu sayede lazer sıcaklıklarından daha düşük seviyede lazer çıkış yüzeyi sıcaklıkları elde ederek yıkıcı optik ayna hasarı (COMD) ortadan kaldırdı. İkinci olarak dağıtılmış dalga kılavuzu (DWG) tasarımı sunuldu. Bu yaklaşımda, lazer bölümleri arasında pasif saydam bölümler oluşturularak ısı dağılımı alanını artırmak amaçlandı. Gösterildiği gibi ısı dalga kılavuzu boyunca dağıtılarak LD sıcaklığı başarıyla azaltıldı. Bu bulgular, ömür ve güvenilirlik açısından önemli ölçüde geliştirilmiş LD cihazları elde etmek ve ısıl yükü yönetmek konusunda rehber niteliği taşımaktadır.

Anahtar sözcükler: Yarı iletken lazer, diyot lazer, yüksek güç, dalga kılavuz tasarımı, yıkıcı optik hasar (COD).

Acknowledgement

First of all, I would like to express my gratitude to my advisor, Asst. Prof. Abdullah Demir, for his unwavering support and exceptional guidance, which have been instrumental in enhancing my knowledge and skills. Additionally, I am thankful to Prof. Alpan Bek and Asst. Prof. Bülend Ortaç for their assistance in reviewing this thesis and providing valuable feedback.

I would like to express my gratitude to the members of the Nanophotonic Devices Laboratory (nanoPhD Lab), namely Yasaman Salimi, Ece Karabey, Eylül Badal, Serdar Şengül, Kaveh Ebadi, Dr. Babak Olyaeefar,Osama Aadil Saadi, Burak Ünal, Enes Şeker, Abdulmalik Abdulkadir Madigawa and Turgay Bebek for making my time here truly enjoyable. And to my dear friends İlayda Özkan and Ebru Buhara for their incredible source of comfort and inspiration. It has been incredible sharing and growing with you all. I want to extend my gratitude to Asst. Prof. Bülend Ortaç for his support in utilizing the optical spectrometer analyzer, which played a crucial role in accurately analyzing our devices. Additionally, I would like to thank to Enes Şeker and Dr. Babak Olyaeefar for their guidance in the cleanroom and to Kaveh Ebadi for his teaching in the characterization lab. I wish to acknowledge the UNAM cleanroom staff; Taha Ilıkkan, Murat Güre, Abdullah Kafadenk, Ergün Karaman and Mustafa Özer for their support.

Last but not least, I wish to express my deepest gratitude to my family, especially my mother Ayşen Sanbur, my grandmother Sevil Sanbur, my siblings Bora and Doğa. Thank you for the love and support.

To My Mother,

Contents

List of Figures

List of Tables

Chapter 1

Introduction

1.1 Laser principle

The achievements of semiconductor laser diodes (LDs) in the last two decades made LDs one of the most demanded devices for many applications, such as optical pumping of solid state and fiber lasers, industrial material processing, telecommunication, and medicine. LDs have the highest conversion efficiency amongst the light sources [2–5]. A Laser (Light Amplification by Stimulated Emission of Radiation) diode acts as a semiconductor optical amplifier inside an optical resonator. A semiconductor optical amplifier is a forward-biased p-n junction fabricated from a direct-bandgap semiconductor material. In a simple configuration, edge-emitting semiconductor laser diodes are cleaved along their crystal plane. The distinct difference in refractive index between the surrounding air and the cleaved crystal results in reflective surfaces along the surfaces called facets. The semiconductor crystal acts both as a gain medium and as a Fabry-Perot optical resonator. An illustration of the system can be seen in Figure 1.1. The feedback inside the resonator is provided with two reflective surface, whereas in a commercial laser diode, the reflectivity of the facets adjusted by mirror coatings, aiming for higher output power through the out-coupled facet with a mirror with lower reflectivity.

In the case of Figure 1.1, reflection relation is $R1 > R2$ where the optical power output is $P_{op1} < P_{op2}$. Band diagram is visible in Figure 1.1, E1 is the valance band and E2 is the conduction level. There are three kinds of transitions between photons and the charge carriers can be seen in the order in Figure 1.1:

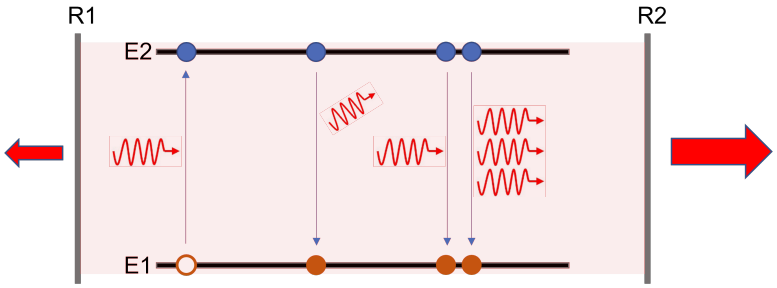

Figure 1.1: Schematic of an optical amplifier with energy states E1 and E2 inside a Fabry-Perot optical resonator with mirror reflectivities of R1 and R2. Transitions inside the energy bands refer to; 1. Optical absorption, 2. Spontaneous emission and 3. Stimulated emission

1. Optical Absorption: Incoming photon with energy equal or higher than the band-gap ($hv \geq E2 - E1$) excites the electron in the E1 state resulting in transition to E2 state, and left behind a hole in the E1 state

2. Spontaneous Emission: An excited electron in the E2 state spontaneously recombines with the hole in the E1 state resulting in the emission of a photon in a random direction.

3. Stimulated Emission: Initially propagating photon inside our cavity stimulates the electrons in the E2 state, resulting in recombination of those electrons while having emission of photons with the same phase and direction as the initial photon. This process is continuous in the cavity with the optical feedback from the mirrors

In order to achieve light amplification or lasing, it is necessary to have a higher population of electrons in the excited states compared to those in the ground state, known as population inversion. This is accomplished by continuously pumping electrons to higher energy levels with a pump source. This pump can be both optical and electrical. Injected carrier concentration (Δn) can be written in terms of injected current density (J) [6]:

$$\Delta n = \tau R = \frac{\tau}{elA} i = \frac{\tau}{el} J \tag{1.1}$$

In the above Equation 1.1, R is the steady-state carrier injection rate, τ is the electron-hole recombination lifetime, e is the electron charge, l is the junction thickness, A is the current injection area and i is the injected current. In an ideal system, the recombination will results in both radiative and non-radiative, for optical amplification, we need to identify the internal quantum efficiency of $\eta_i = \tau/\tau_r$, where τ_r is the radiative recombination lifetime. Peak gain coefficient (g_p) related to transparency charge carrier density(Δn_T) and transparency current density (J_T) can be seen below [6]:

$$g_p \approx \alpha(\frac{\Delta n}{\Delta n_T} - 1) \approx \alpha(\frac{J}{J_T} - 1) \tag{1.2}$$

In Equation 1.2 α represents the absorption coefficient of the active medium. In order to achieve amplification in the gain medium, the current density must exceed the transparency current density ($J > J_T$), where $J_T = \frac{el}{\eta_i \tau_r} \Delta n_T$. Additionally, for amplification to occur inside the resonator, the gain must exceed all losses in the resonator. That includes losses from the output, and the minimum gain required for this condition is known as the threshold gain, denoted as g_{th}. The threshold gain can be calculated using the formula:

$$\alpha_m = \frac{1}{2L} ln(\frac{1}{R_1 R_2}) \tag{1.3a}$$

$$\alpha_r = \Gamma(\alpha_s + \alpha_m) \tag{1.3b}$$

$$g_p \geq \alpha_r, g_{th} \tag{1.3c}$$

The α_m is the optical output losses through the mirrors, where L is the cavity length, R_1 and R_2 are the reflectance of the mirrors, and α_s is the other sources of losses that account for free-carrier absorption, non-radiative recombination and scattering from the optical inhomogeneities. Γ denotes the confinement coefficient indicating the optical power fraction inside the active medium, further increasing the resonator losses. To achieve net amplification, the peak gain g_p must be greater than the losses in the resonator α_r. The laser oscillation condition can also be written in terms of current density:

$$J_{th} = \frac{\alpha_r + \alpha}{\alpha} J_T \tag{1.4}$$

The threshold current density (J_{th}) is function of the transparency current density given in Equation 1.2. Due to both Δn_T and α being temperature dependent, J_{th} is also temperature dependent with the wavelength corresponding to peak gain. It enables control over laser output, modifying output wavelength.

When the current of the laser exceeds its threshold level ($i > i_{th}$), the gain coefficient at its peak, denoted as g_p, becomes greater than the loss coefficient, represented by α_r. This causes stimulated emission to overcome all the losses in the resonator, resulting in the beginning of oscillation and an increase in photon flux, denoted as Φ, with the injected current. The steady-state internal photon flux can be expressed using the equation shown in Equation 1.5.

$$\Phi = \eta_i \frac{i - i_t}{e} \tag{1.5}$$

The photon flux output of the laser, represented as Φ_o, is equal to the product of the internal photon flux, Φ, and the extraction efficiency, denoted as η_e, which is defined as the ratio of the useful light coupled through the output mirror (α_r). The relation of the output photon flux can be seen in Equation 1.6 below:

$$\Phi_o = \eta_e \eta_i \frac{i - i_t}{e} \tag{1.6}$$

The relationship between the laser output photon flux and the injected electron flux above the threshold can be determined by the external differential quantum efficiency, which is shown in the equation presented in Equation 1.7.

$$\eta_d = \eta_e \eta_i = \frac{d(\Phi_o)}{d(i/e)} \tag{1.7}$$

Power conversion efficiency of the laser diode, denoted as *PCE* is defined as the total emitted optical laser power $P_o = \Phi_o h\nu = \eta_d(i - i_t)(h\nu/e)$ to the injected electrical power $P_{elec} = iV$, where V is the applied forward-bias. Then PCE can be written as in Equation 1.8 below.

$$PCE = \eta_d(1 - \frac{i_t}{i})\frac{h\nu}{eV} \tag{1.8}$$

1.2 Thermal effects

The non-optical-energy loss in a laser diode system is converted to heat. This heating power can be found subtracting the total optical power output from the injected electrical power (P_{elec}). We can write the amount of power converted to heat as $P_{heat} = P_{elec} - P_{tot}$ where the total optical power output is $P_{tot} = P_{op1} + P_{op2}$. We should note that the useful power output in the example of Figure 1.1 is P_{op2}.

This heating effect caused by P_{heat} results in higher non-radiative recombination rates, causing a decrease in internal efficiency (η_i). Lower η_i results in an increase in both transparency and threshold current densities (J_T, J_{th}), resulting in less PCE causing even higher heat-loads (P_{heat}). This negative feedback loop causes the self-heating inside the cavity.

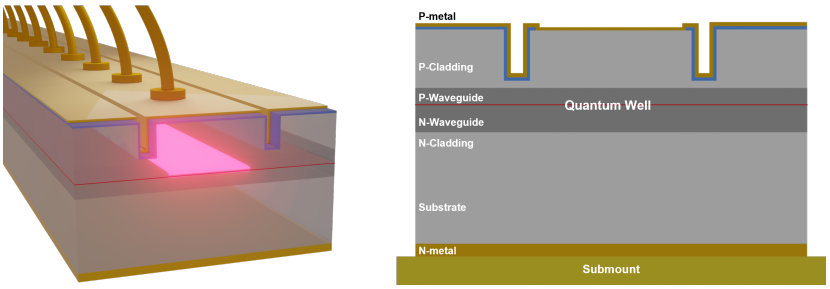

Figure 1.2: An Illustration of a laser diode, highlighted region is the self-heating region of the laser diode.

1.3 Catastrophic optical damage (COD)

The region of heating can be seen in Figure 1.2. In addition to the self-heating mechanism, there is facet heating due to the optical power absorption and non-radiative recombination caused by high-density surface states. This heating leads to critically high temperature values (T_c=120-160°C) that cause irreversible damage called catastrophic optical damage (COD) [7].

Hence mechanisms leading to COD [7–10] and methods towards overcoming the issue with various approaches have been demonstrated; current blocking near the facet, [11, 12] passivation of the surface states, [13–15] non-absorbing mirrors, [16, 17] quantum well intermixing, [18–21] and multi-section waveguide design [1, 22–24].

The process leading to COD begins with an increase in temperature anywhere within the laser cavity, either at the facet or in the bulk of the device. Mechanisms such as surface recombination and surface current play a significant role in the facets. Inside the cavity, the re-absorption of the laser light at the defects can lead to localized temperature elevation. Moreover, the packaging of the device is highly important for the cooling of the LD.

When the temperature is further increased by raising the operation current, heat-sink temperature, or through long-term ageing-induced defects, a critical local temperature (T_c) can be reached. At this point, the thermal runaway is triggered by intrinsic and/or extrinsic mechanisms. An example facet image after COD can be seen Figure 1.3 and Figure 1.4 a).

The intrinsic feedback loop starts with the bandgap shift due to heating inside the

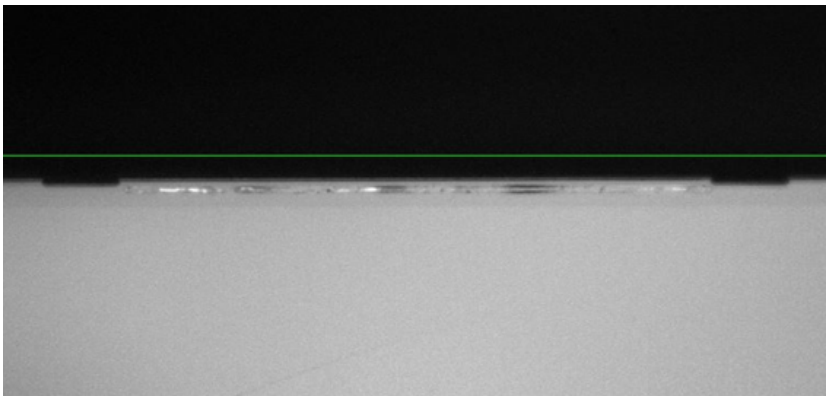

Figure 1.3: Facet image of a high-power GaAs-based LD after catastrophic optical damage.

active region. As a result, interband absorption at the laser emission wavelength increases, leading to a higher density of non-equilibrium carriers. This additional heating, even with a constant fraction of non-radiatively recombining carriers initiates a positive feedback loop.

The extrinsic feedback loop is initiated with the elevated temperatures promoting the accumulation and the creation of defects. The accumulation of defects at the facets or any other active region inside the cavity results in increased absorption of the laser light through defects. Additionally, the higher non-radiative recombination rates in the defect regions further increase the heating.

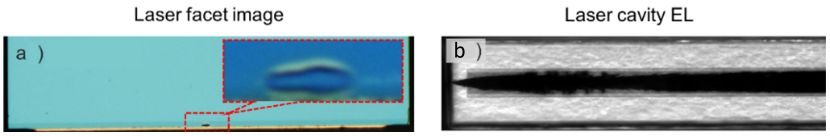

Figure 1.4: a) Optical microscopy image of the facet after catastrophic optical mirror damage (COMD), b) Top electro-luminescence (EL) image of the same LD in a). [1]

The degradation mechanism behind the COD can be separated to three phases [7]:

1. Phase: The temperature at the facet approaches T_c. The duration of this phase (T_f) varies depending on the surface condition of the facet and the operating conditions. It can range from years, gradually increasing temperatures leading to T_c due to material degradation under continuous wave (CW) operation, to a few tens of nanoseconds, where temperature increases occur due to short high-current pulses.

2. Phase: Phenomenon is known as thermal runaway. This phase is characterized by intense localized melting and the resulting "hot spot" expands spatially.

Model calculations indicate that the rise times during this phase are typically between 1 and 10 nanoseconds.

3. Phase: It commences when the thermal runaway ceases due to an energy deficiency. However, further degradation occurs, especially if the operation current is not abruptly terminated. This phase involves the development of collateral damage, such as dark bands (e.g.Figure 1.4, b), which may not be directly associated with the primary damage event. The duration of this phase heavily depends on the operating conditions and can last up to minutes. Typical values for this phase range from microseconds to milliseconds if the operation current remains on. Additionally, collateral damage can continue to evolve over days and weeks until the entire chip is damaged.

Duration described in the first phase (T_f) is described as the lifetime of the LDs and the T_f is an Arrhenius-type function that changes with the activation energy and the operation temperature. The temperature dependence of the reaction rate is typically described by the Arrhenius equation, as shown in 1.9.

$$T_f = 1/rate = A_s \exp(\frac{E_a}{k_b T}) \tag{1.9}$$

In Equation 1.9 the A_s is the scaling factor, E_a is the activation energy (eV), k_b is the Boltzmann's constant (eV/K) and T is the operation temperature (K). Calculated lifetimes in years vs the operation temperatures for varying E_a values can be seen in Figure 1.5. Typical values for E_a vary from 0.3 to 0.7 eV. For industrial level GaAs-based high-power LDs in 9xx-nm, E_a is around 0.64 eV [25], 0.45 eV [26] and 0.28 eV [27] improving chronologicly. Those LDs operate at the device (i.e. junction) temperature around 100 °C. Hence, typical LDs have a median lifetime of around two years when E_a= 0.5 eV.

1.4 Outline

Chapter 1 briefly details Lasers and the mechanisms leading to laser emission. Thermal effects leading to performance deviation and the COD as the fundamental performance limit for LDs.

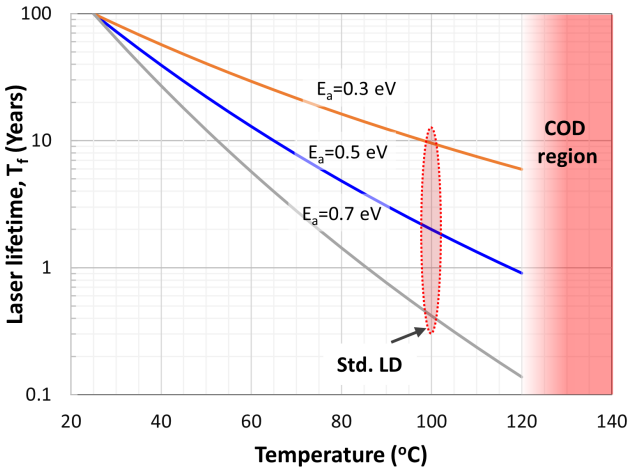

Figure 1.5: Lifetime vs operation temperatures for varying E_a. The red region at 100 $^{\circ}C$ indicates the common operating temperature for a standard (Std.) LD. Gradient red region increasing probability of COD towards higher temperatures.

In Chapter 2, we explain the characterization methods used in this work. Opto-electrical and thermal experimental methods and simulation methods used are explained extensively.

Chapter 3 reveals the waveguide width effect on laser diode characteristics with the methods described in Chapter 2, with the addition of reliability tests performed on the LDs.

Chapter 4 presents and discusses the thermal management of the LDs by two unique waveguide designs. Two-section waveguide design and the Distributed Waveguide (DWG) design.

Chapter 2

Thermal characterization methods

2.1 Experimental

Understanding the heating mechanisms requires precise techniques for thermal characterization of the laser and the facet temperatures, including micro photoluminescence [28], Raman spectroscopy [29], infrared scanning near-field optical microscopy (IR-SNOM) [30, 31], and thermoreflectance spectroscopy (TR) [32–38].

2.1.1 Facet temperature measurement

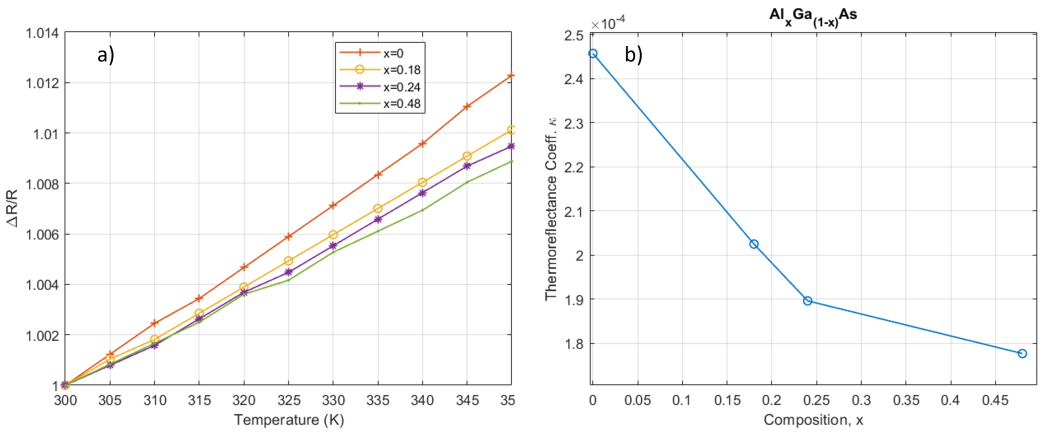

Figure 2.1: a) $\frac{\Delta R}{R}$ vs. temperature (K). Slopes are the thermoreflectence coefficients (κ) for corresponding compositions (x) of $Al_xGa_{1-x}As$. b) Thermoreflectence coefficient (κ) vs the compositions (x) of $Al_xGa_{1-x}As$

In order to quantify the facet temperature of our LDs, the thermoreflectance spectroscopy technique has been employed. Thermoreflectance relation can be seen in Equation 2.1 where R is the reflection coefficient, ΔR is the relative change in reflection, ΔT is the temperature difference, and κ is the TR coefficient, which depends on the material and optical properties of the TR [1, 39]. Calculated $\Delta R/Rvstemperature$ and κ values for varying $Al_xGa_{1-x}As$ compositions can be seen in Figure 2.1. The setup used in our experiments can be seen in Figure 2.2.

$$\frac{\Delta R}{R} = \left(\frac{1}{R} \cdot \frac{\partial R}{\partial T}\right) \Delta T = \kappa \cdot \Delta T \tag{2.1}$$

Equation 2.2 describes the impact of junction temperature (T_{las}) and the temperature increase due to the effects explained in Chapter 1.2 (ΔT_{fac}) on the facet temperature denoted as T_{fac}. It is known from the measurements done sub-threshold current levels, where the P_{op} is effectively zero, thus ΔT_{fac} is zero. As a consequence, the measured T_{fac} is equivalent to T_{las}. [1, 39, 40].

$$T_{fac} = T_{las} + \Delta T_{fac} \tag{2.2}$$

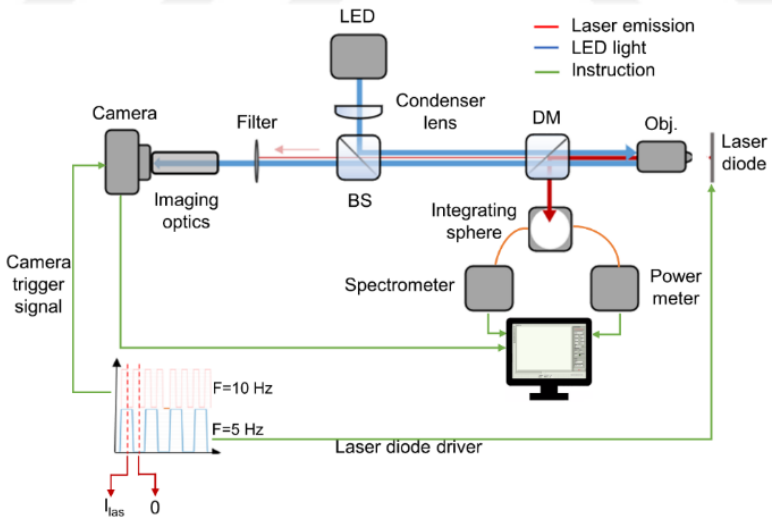

Figure 2.2: The schematic of the thermoreflectance setup [1].

2.1.2 Laser temperature measurement

Laser temperature, also referred as the junction temperature (T_{las}), is measured using the spectral shift method. P_{heat} is the thermal load (W) where it is calculated with the

Equation 2.3(a). I_{las} is the injected current (A), V_{las} is the corresponding voltage (V) and P_{op} is the optical power output (W). Thermal resistance R_{th} (K/W) is calculated with Equation 2.3(b) where the $\Delta\lambda$ is the spectral shift (nm) and λ_T is the temperature dependency on the wavelength(nm/K).

$$P_{heat} = I_{las} \cdot V_{las} - P_{op} \tag{2.3a}$$

$$\frac{\Delta T}{P_{heat}} = \frac{\Delta\lambda / P_{heat}}{\Delta\lambda / \Delta T} \tag{2.3b}$$

$$T_{las} = T_{TEC} + R_{th} \cdot P_{heat} \tag{2.3c}$$

T_{las} is calculated as the reference temperature T_{TEC} (i.e. heatsink temperature) with the addition of change in temperature measured from the wavelength shift. TEC surface temperature is monitored and kept constant at 25°C through the measurements.

2.2 Simulation

Due to experimental constraints, computational tools are widely used to back up the investigation on non-quantifiable attributes. There were both analytical, [41–45] and numerical [46–49] models proposed for this purpose.

2.2.1 3D temperature matching heat-transfer simulation model for thermal characterization

We propose using two tuning parameters to match the temperature profiles and quantify our system's optical absorption and heat dissipation. The employed simulation model uses boundary conditions similar to previously proposed works of Cong et.al. [41] and Jha et. al. [47]. Matching both laser and facet temperatures requires complex models with electrical and optical constants that might not be easy to apply to all material systems. The layer parameters matching with our device structure can be seen in Table 2.1.

In this work, we utilize a thermal simulation model to fit the three-dimensional temperature of the LDs that requires simple electro-optic characterization, facet temperature (T_{fac}) and laser temperature (T_{las}) measurements to understand the heat dissipation

Table 2.1: Layer parameters for the LDs used in the simulation model

Layer	Material	Thermal Cond. (W/m·K)	Heat Cap. (J/kg·K)	Density (kg/m^3)	Thickness (μm)
P-metal	Ti\Pt\Au	145	171	6000	0.9
P-contact	GaAs	55	330	5320	0.1
P-cladding	AlGaAs	10.4	387.6	4571	1.2
P-waveguide	AlGaAs	24.9	351.6	5039	0.3
Quantum well	InGaAs	-	-	-	-
N-waveguide	AlGaAs	24.9	351	5039	0.8
N-cladding	AlGaAs	18.4	358.8	4946	2.3
Substrate	GaAs	55	330	5320	100
N-metal	AuGe/Ni/Au	87	20	2000	1.1
Solder	AuSn	57	150	14509	5
Submount	AlN	220	600	3255	400
Metallization	Ti\Pt\Au	53.4	171	6000	0.8
Solder	SnAgCu	33	230	7360	10
TEC Boundary	-	-	-	-	-

mechanisms. By utilizing the simulation tool, narrow and broad waveguide LDs are compared to investigate their heat-transfer characteristics. Hence, we can identify the relation between the reliability and the waveguide width (W) in the next chapter (Chapter 3).

All external surfaces are considered adiabatic boundaries except for the convective boundary condition at the thermo-electric cooler (TEC) surface. Natural convection was found to be negligible ($H \approx 5$ W/m^{2}K). The simulation model considers only junction heating due to the self-heat of the LD and output facet heating due to optical absorption.

2.2.2 Convective heat transfer boundary condition

The convective heat transfer boundary condition (BC) models the cooling of the system by limiting the heat output through the boundary. This approach has been shown to be more accurate in the simulations of LD heating [41,42] compared to the use of constant temperature BC, which assumes an infinite heat dissipation rate (e.g., $H = \infty$). The convective heat-transfer BC is applied to TEC boundary, and heat-flux out of boundary (Q_{out}) is given by Equation 2.4:

$$Q_{out} = H \cdot A \cdot (T_s - T_{TEC}) \tag{2.4}$$

Where H is the convective heat transfer coefficient (W/m^{2}K), A is the surface area (m^2), T_s is the surface boundary temperature and T_{TEC} is the TEC boundary temperature (i.e., 25°C). The convective heat transfer BC is a way to alter the R_{th} of the device.

$$R_{th} = R_{th,cond} + R_{th,conv} \tag{2.5a}$$

$$R_{th,cond} \approx \frac{thickness}{k \cdot area} \tag{2.5b}$$

R_{th} of the system can be explained in two parts; conductive thermal resistance $R_{th,cond}$ and convective thermal resistance $R_{th,conv}$ (Equation 2.5a). As in Equation 2.5b, $R_{th,cond}$ is defined by the thermal conductivity (k) and the LD geometry (thickness and area), but $R_{th,conv}$ can be tuned using convective heat transfer coefficient H.

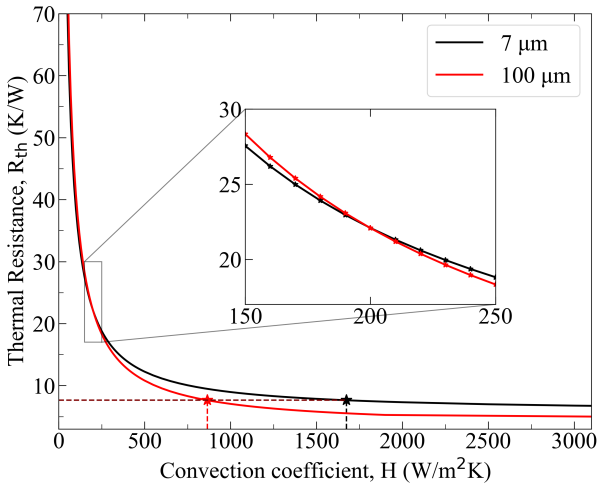

Figure 2.3: Thermal resistance vs. convection coefficient. The dashed line indicates the LD's experimental R_{th} value of 7.6 (K/W). The inset shows the transition point at H=200 (W/m^{2}K)

In Figure 2.3 effect of convection coefficient, (H) on the thermal resistance, (R_{th}) can be seen for both LDs with different waveguide widths. For $H < 200$ W/m^{2}K, systems heat dissipation is limited by the convective characteristics ($R_{th,conv}$) and for $H > 200$ W/m^{2}K the conductive characteristics ($R_{th,cond}$) becomes dominant. Both LDs fall into the second region where the $R_{th,cond}$ limits the R_{th} mostly. 7 µm LD shows higher conductive thermal resistance across $R_{th,cond}$ limited region due to its smaller active area of heat flux going towards the heatsink, e.g. in Equation 2.5b shows higher overall $R_{th,cond}$ for given H. We note that simulation R_{th} is not a function of heat load since there is no temperature dependency defined.

Convective heat transfer boundary condition at the TEC surface reduces the R_{th} as H increases. Since it is the only source of heat output, it allows the R_{th} and T_{las} of

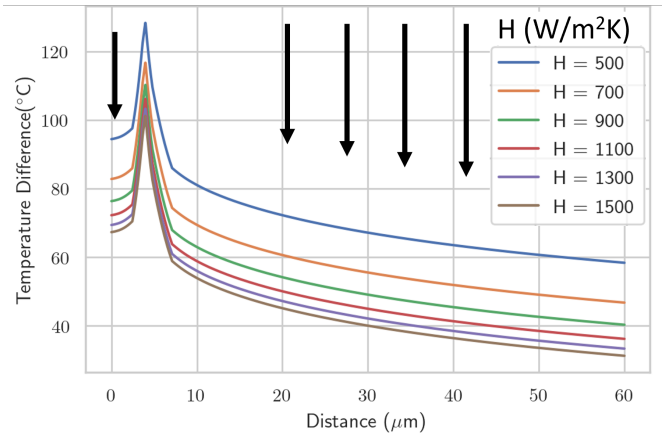

Figure 2.4: Convection coefficient (H) effect on the temperature profile of the laser facet. Facet absorption is kept constant at A=%0.7.

the system to be fitted to the experimental values. Markers in Figure 2.3 indicates corresponding H values for the experimentally measured R_{th} of 7.6 K/W. You can see the effect of H on the facet temperature profiles with a constant A in Figure 2.4.

2.2.3 Facet absorption

Facet temperature is matched with the experimental results using a 2D heating boundary condition that matches the quantum well area on the facet [47]. The optical absorption fraction is calculated with Equation 2.6 where A denotes the absorption fraction of the total optical power P_{tot} and P_{op} is the measured optical power output.

$$A = 1 - \frac{P_{op}}{P_{tot}} \tag{2.6a}$$

$$P_{tot} = P_{op} + P_{abs} \tag{2.6b}$$

2.2.4 Validation of the simulation model

To validate the model, a laser diode was utilized at a low operating current of 2A to prevent overheating, and two sets of parameters were tested. One with the TEC on and the other with TEC off. It is worth noting that any change in optical power output was negligible and had no significant impact on the validation process. The main objective of the experiment was to observe any change in the convection coefficient under the two different parameter sets, with the optical power absorption remaining constant, as

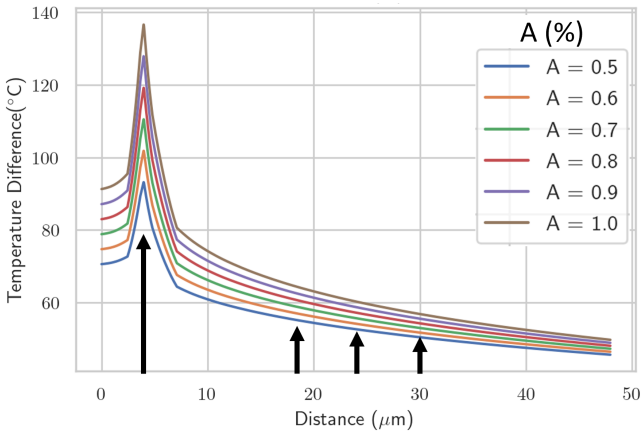

Figure 2.5: Effect of absorption fraction on facet temperature profiles. Convection coefficient is kept constant at H= 1100 W/m^{2}K

demonstrated in Figure 2.6. It is apparent that the temperature increase due to lack of cooling from the TEC directly translates to a decrease in the convection coefficient (H).

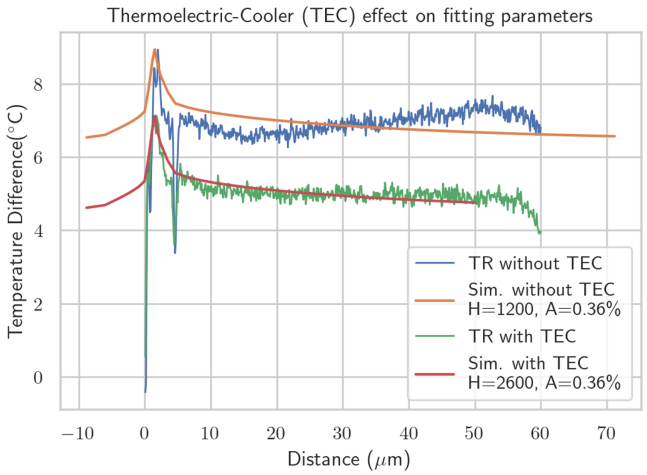

Figure 2.6: Two sets of experiments where a laser diode operating at a low current of 2A: One with TEC turned on and one with TEC turned off. Thermoreflectance Spectroscopy results and simulation model fits can be seen with the respected fit parameters of H=1200 W/m^2 for TEC off and H=2600 W/m^2 for TEC on where the optical power absorption fraction remains at a constant value of A=%0.36.

2.2.5 Effect of Joule heating on the temperature profile

The effect of Joule heating on the temperature profiles and fitting parameters is investigated by calculating the heat-load ($P_{heat,joule}$) corresponding to each layer in the body defined using the Joule-Lenz law stated in Equation 2.7. Heat load assumed to

be vertically aligned with the waveguide, and the contribution percentages can be seen In table.2.2.

Table 2.2: Calculated $P_{heat,joule}$ contribution over the LD layers.

Layers	Contribution
P-contact	∼0%
P-cladding	4.9%
P-waveguide	5.1%
Quantum well	∼0%
N-waveguide	1.4%
N-cladding	5.3%
Substrate	87.8%

$$P_{heat,joule} = I^2 \cdot R \tag{2.7}$$

The effect of $P_{heat,joule}$ on the facet temperature profile can be seen in Figure 2.7. The result indicates a lower T_{facet} because of the total P_{heat} is not more distributed among all the layers rather than previously confined in the active region only. The difference in temperature is negligible with no significant effect on fitting parameters, it is found to be negligible and omitted to keep the model simple.

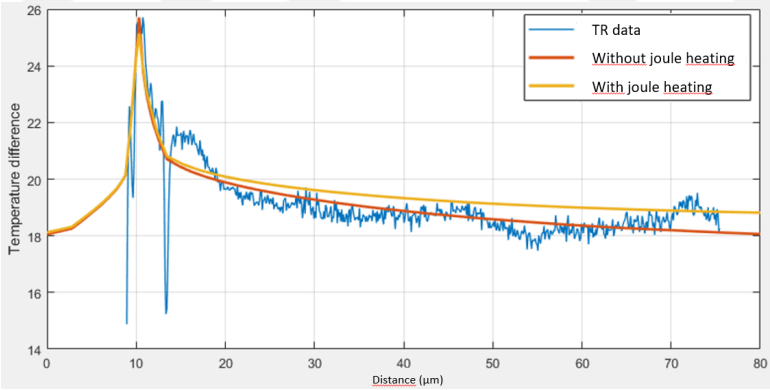

Figure 2.7: Effect of $P_{heat,joule}$ on simulated facet temperature profile.

Chapter 3

Waveguide width effect on laser diode characteristics

3.1 Performance

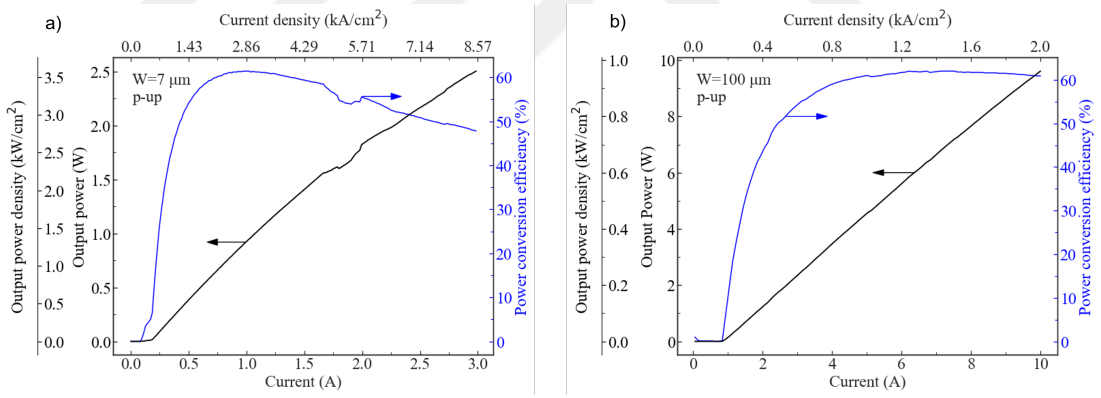

Figure 3.1: Power and power conversion efficiency vs. injection current for LDs with cavity lengts of 5mm and waveguide width of, **a)** 7 µm and **b)** 100 µm. The top and left-most axes indicate the current and output power densities, respectively.

We have investigated two epi-up, high-efficiency, single quantum well, 5 mm long AlGaAs/GaAs-based LDs [50] with different waveguide widths of 7 and 100 µm. They have the same thermal resistance (R_{th}) value of 7.6 K/W. Figure 3.1 shows the LI-PCE characteristics of the LDs. Both LDs have similar PCEs of %60 at maximum. 7 µm LD has 3.5 times higher output power density and 4.2 times higher current density compared to 100 µm LD. In Figure 3.1, a) sudden shift of power around 1.8A is a result of the higher order optical mode starting lasing.

3.2 Thermal Characterization

T_{fac} and T_{las} variation with laser self-heat density can be seen in Figure 3.2 for both LDs. In Figure 3.2, the square and circular markers indicate experimental results for 7 and 100 µm LDs, filled and empty markers display T_{fac} and T_{las} where the dashed lines are simulation results. Despite having a much higher self-heat density, LD with the 7 µm waveguide width displays much lower temperatures for both T_{las} and T_{fac}.

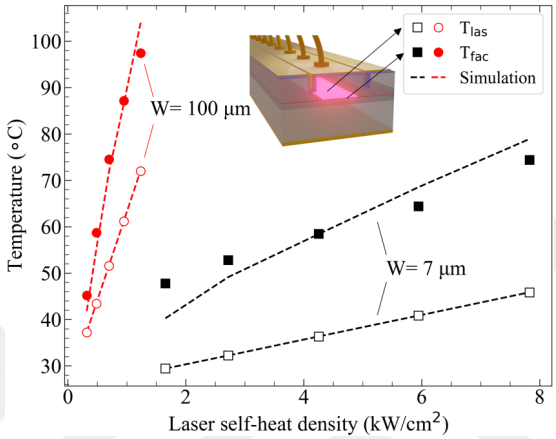

Figure 3.2: Experimental and simulation results of T_{fac} and T_{las} vs. laser self-heat density. The inset image illustrates laser self-heating.

We first fitted experimental R_{th} and T_{las} values with our simulation model using the convective heat-transfer boundary condition to analyze the characteristics further. T_{fac} was fitted with a single absorption fraction selected to result in the least standard deviation across all data points. Simulations resulted in absorption fractions of %0.011 and %0.045 for 7 and 100 µm, respectively. Due to the absence of passivation coating on the 100 µm laser, the absorption fraction is significantly higher than the 7 µm with the passivation coating [15]. Our findings indicate lower absorption values in comparison to the prior study by Jha et al. [47]. Jha et al. utilized a model in which heat dissipation was regulated through a constant temperature boundary condition, resulting in lower overall R_{th} without the inclusion of $R_{th,conv}$. Introduction of $R_{th,conv}$ leads to higher T_{las} and ultimately requires less P_{abs} to achieve temperatures consistent with the experimental data.

The Figure 3.3 displays temperature maps of the facets obtained through experiment and simulation for 7 µm and 100 µm width LDs in a) and b), respectively. 100 µm LD exhibits a decrease in facet temperature on the right-hand side of the temperature maps due to the placement of the cooling fan in the TR setup.

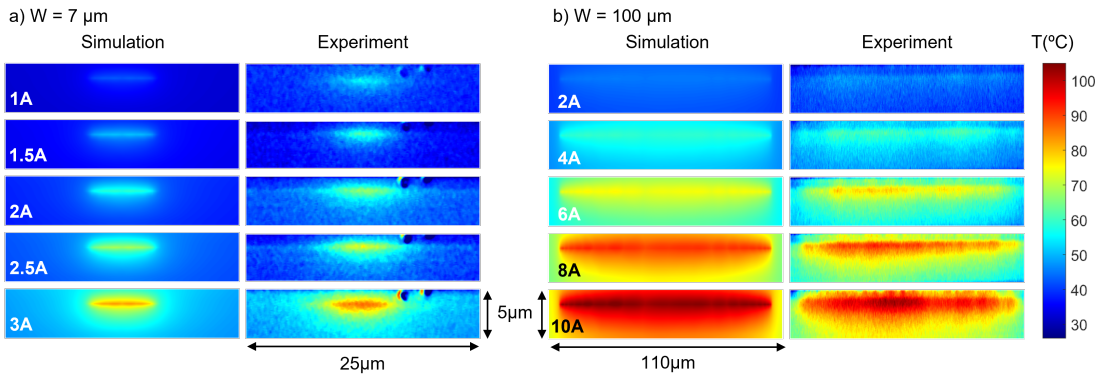

Figure 3.3: Facet temperature maps for simulation and experiment of LDs with the waveguide widths, **a)** 7 µm and **b)** 100 µm.

3.3 Reliability

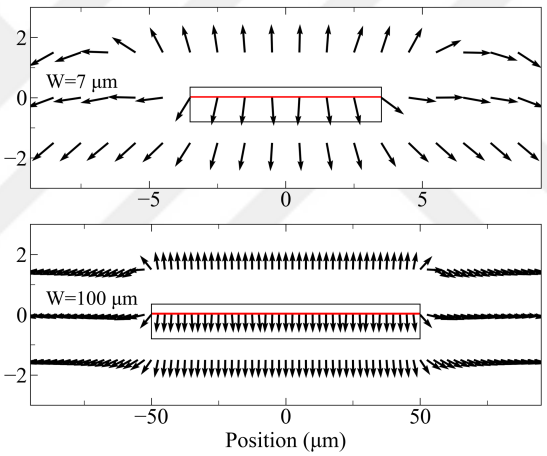

Figure 3.4: Average heat-flux maps of LDs with the waveguide widths, **a)** 7 µm and **b)** 100 µm.

Looking at the heat-flux maps given in Figure 3.4, it is visible that 7µm LD have significantly higher lateral heat-fluxes. The temperature profiles in Figure 3.3 and the heat-flux maps given in Figure 3.4 of LDs strongly depend on their waveguide widths, suggesting a significant impact on reliability. To investigate further, we performed high current testing and failure analysis on LDs with a cavity length of 5 mm and waveguide widths ranging from 7 to 222 µm. Three LDs were tested for each width. These LDs were tested beyond their power rollover levels to assess maximum output power and laser self-heat densities, as illustrated in Figure 3.5.

Our results, presented in Fig.3.5, illustrate the relationship between the width of the waveguide and laser self-heat density and maximum output power densities. The filled

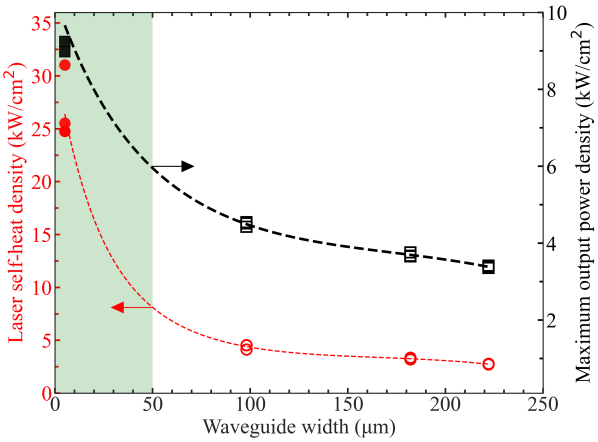

Figure 3.5: Failure test results, self-heating density, and maximum output power density vs waveguide widths of LDs. Filled markers indicate COD-free operation. The green zone indicates the more reliable narrow waveguide region

markers represent devices that exhibited COD-free operation. The 7 μm LD displayed COD-free operation despite having significantly higher maximum output power and heat-load densities. The thermal characterizations, as illustrated in Fig.3.2 and 3.3, further support our findings of COD behaviour of narrow waveguide LDs, with lower temperatures observed for the LDs with narrower waveguides.

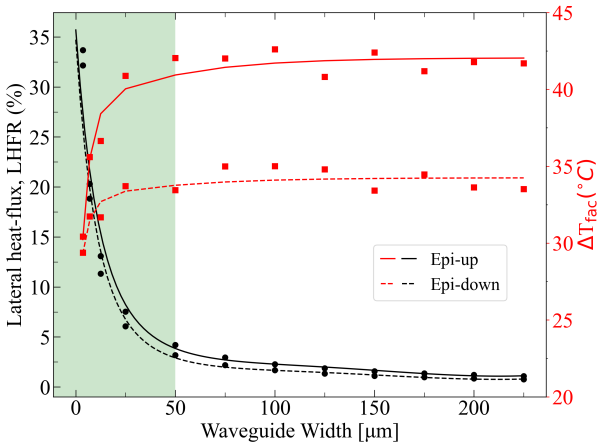

Figure 3.6: ΔT_{fac} and lateral heat-flux ratio (LHFR) for varying waveguide widths. Solid lines are epi-up, and dashed lines are the epi-down configurations. Black lines show the LHFR. Red lines show the maximum temperature increase at the facet. The green zone indicates the transition from the wide to narrow waveguide of thermal characteristics.

In order to understand the superior thermal characteristics of the narrow waveguide width LDs, we looked at the heat-flux maps of previously simulated LDs with waveguide widths of 7 μm and 100 μm can be seen in Figure 3.4, as expected, the lower W LD displayed much higher lateral heat flux. We examined the 3D heat flow for varying waveguide widths. We found that the heat flux was higher in the lateral direction for

the narrow LDs. We have run simulations with a constant H value of 1000 W/m^{2}K, the constant heat-load density of 10 W/mm^2 and constant P_{abs} density of 0.01 W/µm^2 selected parameters decided on the average of all measured values as a reference frame. Results of the simulation can be seen in Figure 3.6

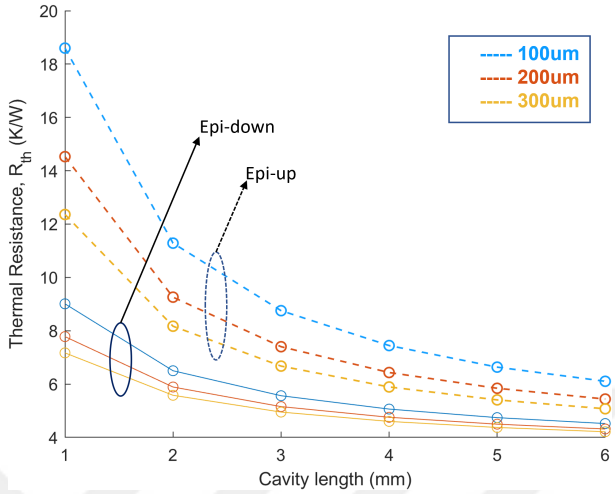

Figure 3.7: Epi-up and epi-down thermal resistance vs varying cavity lengths, where the blue, orange and yellow lines correspond to waveguide widths of 100, 200 and 300µm, respectively.

Figure 3.6 depicts the impact of waveguide width on the thermal resistance (R_{th}) and the lateral heat-flux ratio out of the waveguide region. Our findings show that the epi-down configuration results in lower R_{th} as the effect of waveguide width on R_{th} is also less pronounced. Additionally, an increase in the area of heat dissipation leads to lesser $R_{th,cond}$. We observe that the lateral heat-flux ratio (LHFR) approaches to a minimum as the waveguide width increases, leading to a maximum value of ΔT_{fac}. Notably, the point of convergence of the LHFR out of the waveguide width of 50 µm can be considered the transition point from narrow to broad waveguides regarding reliability and thermal properties.

The effect of cavity length on R_{th} is simulated with the same parameter sets. The R_{th} vs. varying cavity lengths can be seen in Figure 3.7 resulted in decreasing R_{th} values as the cavity length increases. Also, the effect is more pronounced for the epi-up configuration since the $R_{th,cond}$ is higher due to the distance of heat dissipation.

Chapter 4

Thermal management of LDs by waveguide design

The concept behind employing electrically isolated sections is to have precise control over the injected current in various regions of the LD waveguide. This control is essential for regulating the gain and managing the heat-load distribution throughout the device. By incorporating these isolated sections within a monolithic structure, the LD can achieve exceptional thermal characteristics with a simple approach.

In order to achieve electrical isolation, the highly doped layers between sections are etched, and then the area is coated with a dielectric insulator. Channel depth is optimized to prevent optical losses while providing the maximum amount of electrical resistance. The sections can be separately pumped with different current sources with different operation modes and current levels.

4.1 Two-section waveguide design

The previously established design aims to move the T_{las} away from the facet by introducing the isolated section in front of the output facet [1, 39, 51]. Schematics of the design can be seen in Figure 4.1, where the gain and temperature profiles indicate isolated heat generation of the active section.

In this design, fabricated GaAs-based 915 nm LDs were used with waveguide widths of 100 µm and a total cavity length of 5 mm combined with both passive and active

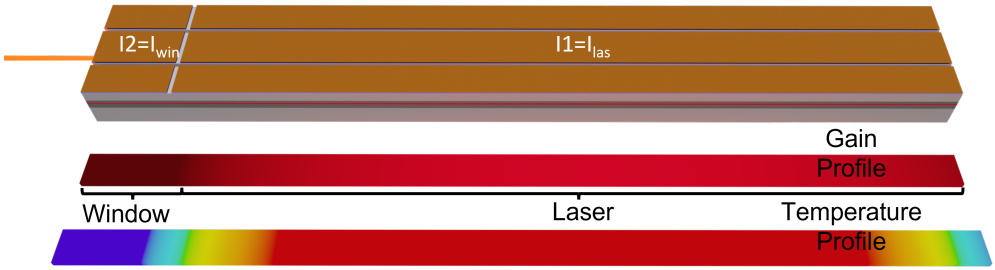

Figure 4.1: 3D model of the two-section laser diode with the corresponding gain and temperature profile.

sections. Different section lengths of $L_{win} = 0, 250, 500, 1000, 1500$ µm were studied systematically.

4.1.1 Characterization

First, characterization was done with $I_{win} = 0$ mA, and subsequently, their behaviour was examined with respect to injected win current (I_{win}). Finally, we focus on the two-section LDs with window lengths of 500 and 1000 µm, which exhibited the best performance, and compared them to the standard LD ($L_{win} = 0$ µm) by conducting failure tests.

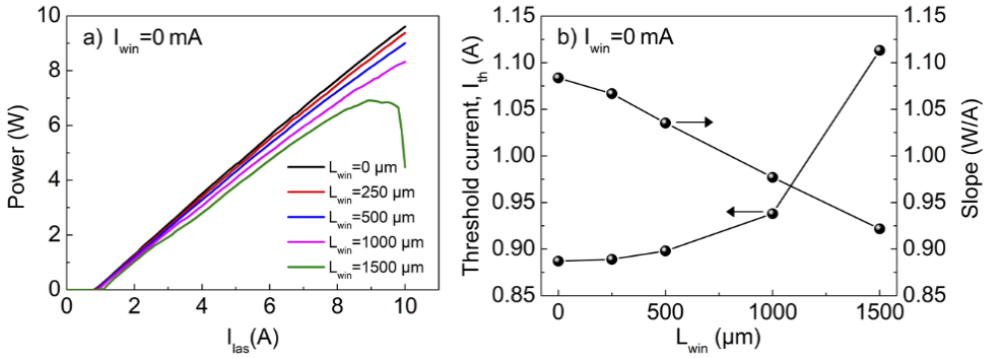

Figure 4.2: Experimental results in continuous-wave operation at 25°C. a) Power vs. current curves for varying L_{win} structures. b) threshold current and slope vs. L_{win}

The measured CW L-I data in Figure 4.2 with $I_{win} = 0$ demonstrates a reduction in output power as L_{win} increases. The slope decreases linearly with longer L_{win}, indicating increasing absorption losses due to an increase in unpumped region length. Further increase in L_{win} to 1000 and 1500 µm results in a significant increase in I_{th} indicating that the loss influence is stronger compared to the shorter cavity length.

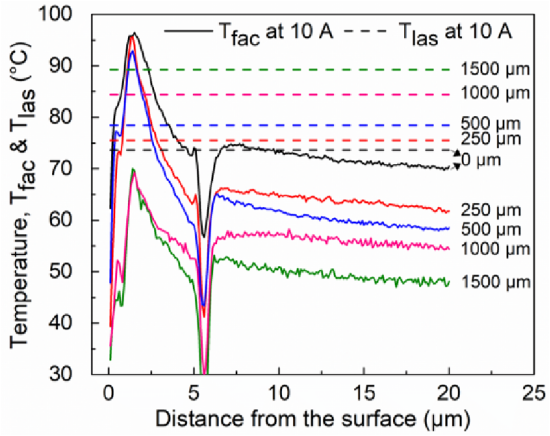

Figure 4.3: Vertical temperature scan displays the measured facet temperature maps, T_{fac} vs. distance from the top surface and T_{las} for I_{las} =10 A.

Figure 4.3 demonstrates that, for all two-section LDs, the average and peak temperatures of the facets are lower than those of the standard LD (L_{win} =0). Importantly, even the peak temperature at the facet, T_{fac} is lower than the temperature at the laser section (T_{las}) for designs with L_{win} = 1000 and 1500 µm. Comparing these two designs reveals comparable peak T_{fac} values, indicating that an L_{win} = 1000 µm is sufficiently long to isolate the heat generated by the laser section from the facet.

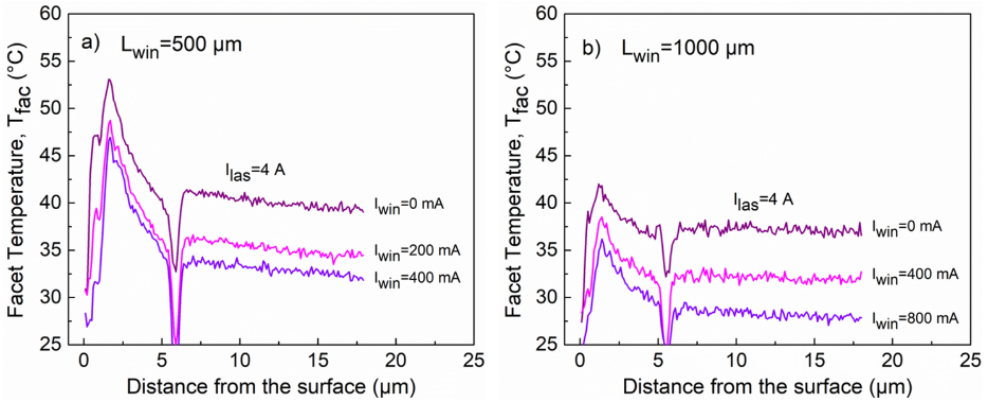

Figure 4.4: Comparison of facet temperature profiles is conducted for two-section LDs at I_{las} = 4A, considering two different scenarios: a) L_{win} = 500 µm with varying injection currents I_{win} of 0, 200, and 400 mA, and b) L_{win} = 1000 µm with varying injection currents I_{win} of 0, 400, and 800 mA.

In Figure 4.4, the facet temperature (T_{fac}) of LDs with L_{win} =500 and 1000 µm is compared at I_{las} =4 A. It can be observed that injecting I_{win} reduces facet temperatures for both LDs while increasing the optical power output. The results of the output power and the T_{fac} validate that properly pumping the window section under suitable L_{win} condition effectively recovers the power degradation and further cools the LD facet.

Finally, when examining the failure characteristics of the two-section LDs in comparison to the standard LDs, a COMD (Catastrophic optical mirror damage) point becomes evident in the epitaxial layer which can be seen in Figure 4.5 (a1). The top electroluminescence (EL) image in Figure 4.5 (a2) reveals the presence of the dark line defects extending from the COMD point on the front facet towards the laser cavity, indicating a typical COMD behavior for standard LDs (i.e., $L_{win} = 0$) [52].

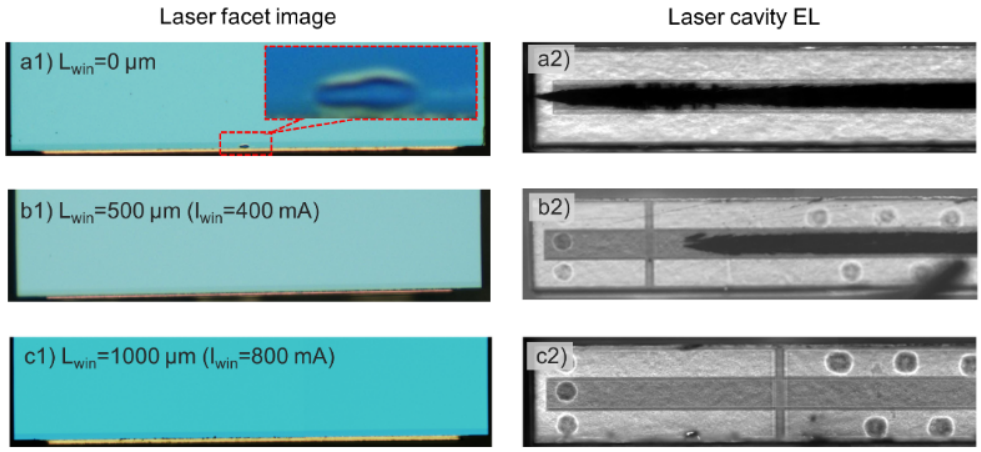

Figure 4.5: The optical microscope image displays the LD facet, while the top EL image reveals the laser cavity condition after conducting 20 A, continuous-wave, and 20-degree Coverdrive tests. Panels a1-2, b1-2, and c1-2 correspond to three different L_{win} values: 0 µm, 500 µm, and 1000 µm, respectively.

For LDs with L_{win} =500 µmu and I_{win} =400 mA, the maximum power(current) achieved is 13.6 W(15.5A), which is 0.5W higher than that of the LD with L_{win} =0 µmu. Under optical microscopy, Figure 4.5 (b1) illustrates that the front facet appears clear without any visible COMD blister. However, the EL image reveals the presence of catastrophic optical body damage (COBD) in the laser section, distinct from the window section, as shown in Figure 4.5 (b2). Figure 4.5 (c1-2) provides visual evidence of the laser output facet and internal structure, confirming that the operation of the LDs are free from COMD. Under these optimized conditions, the two section LDs with L_{win} =500 and 1000 µm exhibit similar output power levels to the standard LD with L_{win} =0 µm. However, the two-section LDs have higher current densities and higher T_{las} (the temperature at the laser section) for a given I_{las} due to the shorter L_{las}, while the total length remains the same for all LDs. The higher current densities in the two-section LDs make them more susceptible to COBD. This is demonstrated for L_{win} =500 µm; however, it is confirmed that both window lengths operate without COMD.

4.2 Distributed waveguide design

We have examined the performance of two-section LDs and compared it to a standard LD, focusing on LIV characteristics, output facet temperature, and COMD results. Based on our understanding of these measurements and outcomes, we have chosen to implement and investigate the application of passive sections along the waveguide. The purpose is to effectively distribute the heat load across the waveguide, ultimately reducing the overall temperature and increasing the device's reliability.

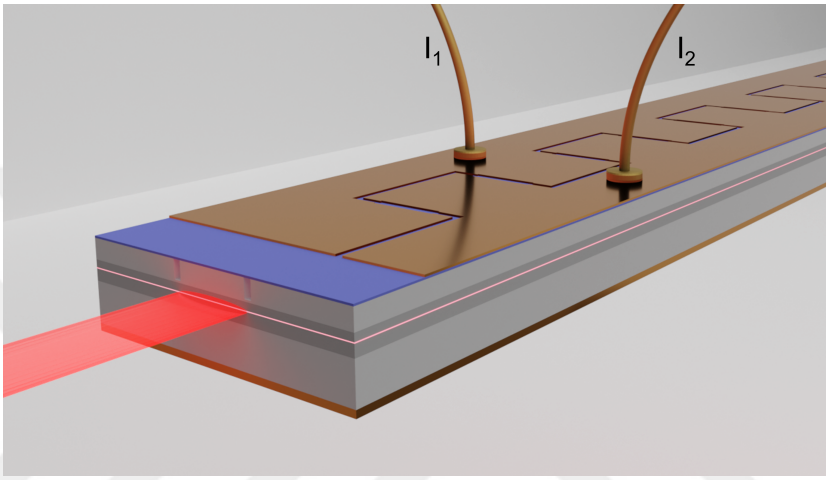

Figure 4.6: Illustration of a distributed waveguide laser diode (DWG-LD). Separate current injections of I_1 (i.e., I_{las}) and I_2 (i.e., I_{pas}) is visual.

4.2.1 Device design

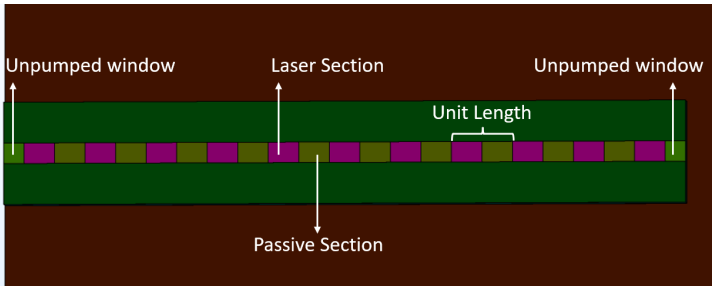

Figure 4.7: Top view of our simulation model where the unpumped windows near the facets, active sections, passive sections and section lengths are visible.

Considering the learnings of two-section waveguide design, we know that the current density across designs affects the body temperature. Therefore it also translates to the facet temperatures, e.g. Equation 2.2. To achieve one to one comparison where there are no additional effects to consider, we decided to have the same active pumping area

with a standard LD (Std. LD) and the active sections to be located at the same distance to the LD facets.

4.2.1.1 Simulation

To gain insights into the thermal characteristics and determine the most effective device parameters, our approach involved examining our device using two specific variables:

- **Fill factor** (FF); Laser section area divided by the total device area, which can be defined as $FF = L_{las}/(L_{las} + L_{pas})$.
- **Laser length** (L_{las}); A single laser length which can seen in Figure 4.7.

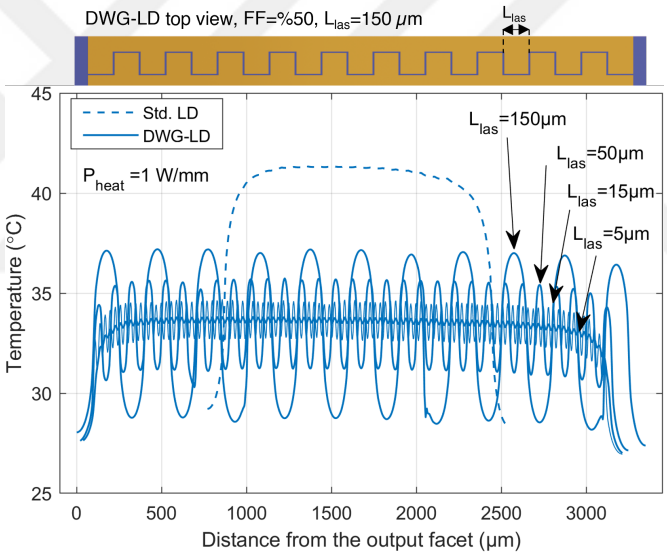

Figure 4.8: Simulated temperature profile comparisons for epi-up 1.5 mm Std. LD vs 3 mm DWG-LD of FF of %50 with varying laser lengths at P_{waste} = 1 W/mm. A top view model representing a DWG-LD with SL= 300 μm matching the x-axis is present on the top side.

We employed the Comsol Multiphysics heat-transfer module to create a simulation model, utilizing the geometrical properties outlined in Table 2.1. To represent a typical high-power LD (laser diode), we set the waveguide width (W) to a fixed value of 100 μm. Additionally, we established the heat-load density per active pumping length as 1, 2.5 and 4 W/mm, which was chosen as the low, median and high operating points based on our previous test results in Chapter 3. In the simulations, the initial and heat-sink temperature was set to be 25 °C.

For quantitative comparison between design parameters, a reference frame is selected with active laser length of 1.5 mm. A 1.5 mm Std. LD vs 3 mm DWG-LDs for FF of %50. The temperature profiles across the waveguide can be seen in Figure 4.8 for Std. LD and DWG-LD with L_{las} of 5, 15, 50 and 150 µm. A temperature decrease for all DWG-LDs are visible compared to standard LDs. The ideal case seems to have L_{las} smaller than 5 µm with the nearly uniform temperature profile. Notably, the thermal crosstalk between laser and passive sections increases as the unit length decreases, leading to a more uniform temperature profile and lower temperatures for the laser sections.

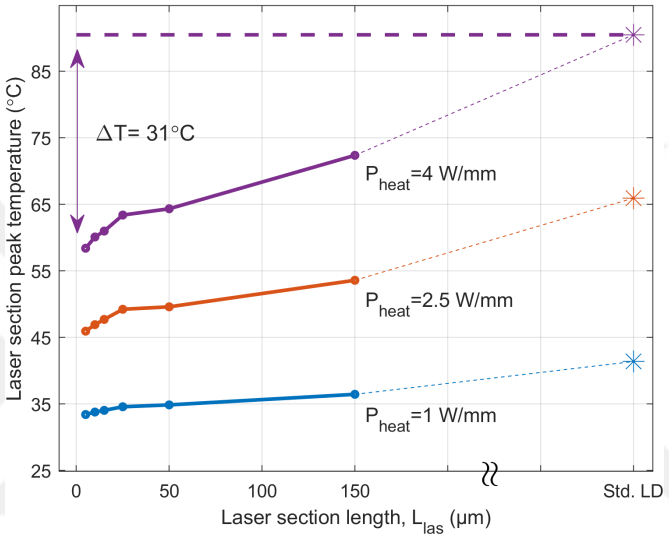

Figure 4.9: Laser section peak temperatures for varying section lengths and heat-load densities. The axis is cut and the last marker with the dashed lines represents the Std. LD with the same P_{waste}. It is evident that there is a temperature advantage of 31 °C when the P_{waste}= 4 W/mm.

Effect of heat-load densities on laser section peak temperatures for varying L_{las} can be seen in Figure 4.9. Showing increasing temperature difference comparing DWG-LD and Std. LD with maximum of 31 °C when the P_{waste}= 4 W/mm. Looking at the temperatures advantage in the simulation, the decrease in temperature of the DWG-LDs effects the lifetime of the samples 5 to 10 times higher than those Std. LDs. can be seen in Figure 4.10.

4.2.2 Fabrication

We utilized a high-efficiency GaAs-based epitaxial structure with a single quantum well (QW) active region [53]. Before deciding the fabrication parameters such as L_{las}

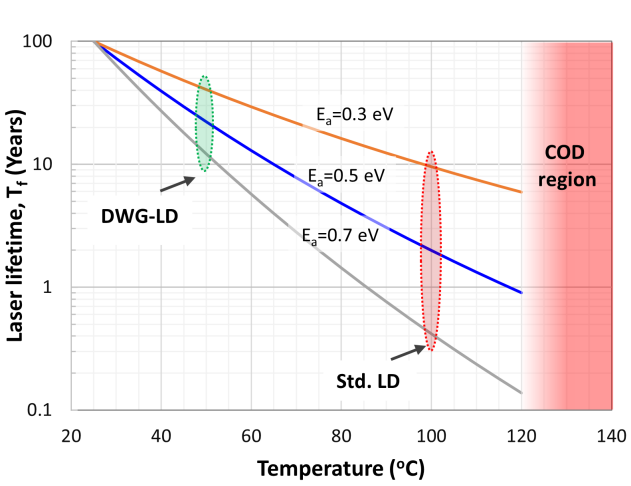

Figure 4.10: Lifetime vs operation temperatures for varying E_a. The red region at 100 ^{circ}C indicates the simulated operating temperature for a standard (Std.) LD and the green region represent the DWG-LD operating temperature in the simulations. Gradient red region increasing probability of COD towards higher temperatures.

and FF, we need to consider each fabrication step carefully to implement the optimum design parameters.

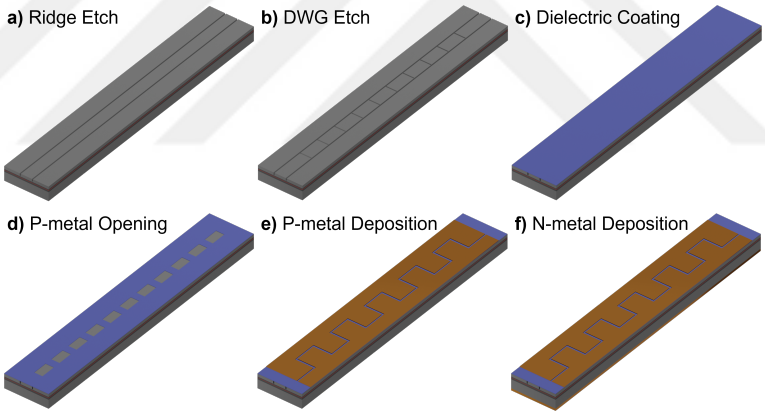

Figure 4.11: Illustration of basic fabrication steps: a) Ridge etch, b) DWG etch, c) Dielectric coating, d) P-metal opening, e) P-metal deposition, f) N-metal deposition.

The fabrication process steps of DWG-LD are illustrated in Figure 4.11; a) Ridge etch: Applied to create lateral confinement for optical modes by forming a refractive index difference. b) DWG etch: Primarily etching the high-doped region to create electrical isolation between the laser and passive sections. c) Dielectric coating: Creating electrical isolation throughout the surface. d) P-metal opening: Etching of the dielectric coating on the desired sections to control the electrical injection areas. e) P-metal deposition: Metal deposition followed by lift-off to create a contact on the p-side. f) N-metal deposition: Metal deposition for the n-side contact.

Considering the simulation results, shorter laser sections is beneficial for lower laser

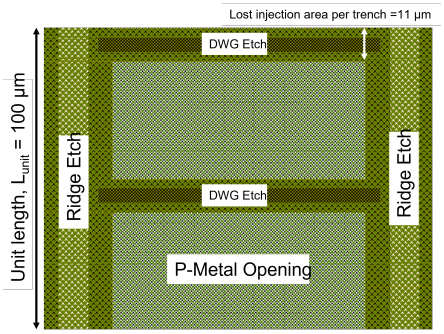

Figure 4.12: A unit section showing three layers (Ridge-etch, DWG-etch and P-metal opening) in the mask design overlapping for a section with FF=%50 and L_{las}=50 µm.

temperatures and more uniform distribution. However, during the fabrication, each boundary between sections requires etching for electrical isolation that will lead to non-uniform current injection and higher threshold current levels compared to a standard LD. Considering the tolerance of our lithography, there is a trade-off between the injection area and the shorter laser section lengths. Each section requires two etching zones that have tolerances for DWG-etch, P-metal opening and the lift-off prior to the p-metal deposition to remove the metal deposited between sections. A unit section on our mask design showing the lost injection area can be seen in Figure 4.12 with a section length of 100 µm. In the figure, it can be seen that for the given section length $\sim$ %20 of the injection area is deprived.

4.2.2.1 Mask Layout

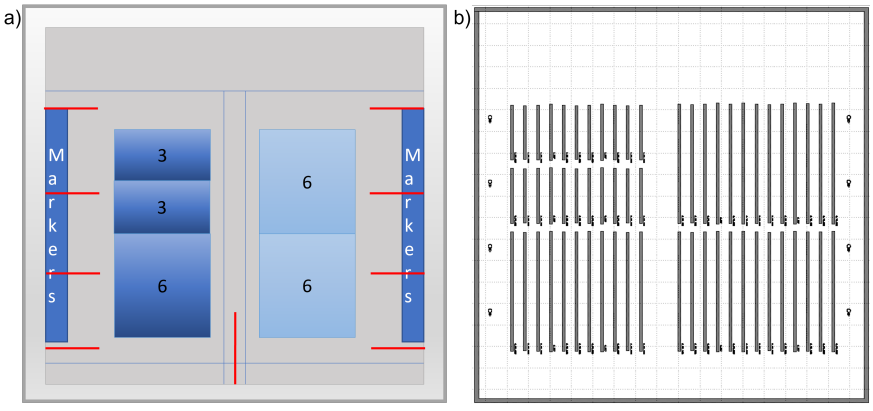

Figure 4.13: a) Schematic of the mask layout and b) the cap-layer mask design as an example.

UV lithography with chrome masks is a technique in semiconductor manufacturing, enabling precise patterning processes. It involves coating the substrate with a photoresist layer and aligning a chrome mask containing the desired pattern to ensure accurate

pattern transfer. UV light passes through transparent regions of the mask, exposing the photoresist and causing a chemical reaction. Exposed areas are selectively removed during development for a positive photoresist, leaving behind patterned areas on the substrate.

Our mask design consists of two 3mm and three 6mm bars. Bars consist of Std. LDs and DWG-LDs with fill factors of %50 and unit lengths of 100, 200, and 300 µm. The layout can be seen in Figure 4.13 a) where the numbers are the cavity lengths, red lines indicate the cleave zones and the sides have markers to align the consecutive steps. b) the cap layer mask is visible as an example. In this process, we have a total of seven masks with six alignment processes.

4.2.2.2 Process

Cap layer etch

In the epitaxial design, we incorporate a 100 nm layer of heavily doped gallium arsenide (GaAs) cap. The cap layer etch is implemented by chemical etching, using a mixture of phosphoric acid (H_3PO_4) diluted with hydrogen peroxide (H_2O_2). To facilitate wafer oxidizing, hydrogen peroxide is added to the etchant solution. Subsequently, the highly doped GaAs cap is etched away in 20 seconds, as depicted in Figure 4.14. The same etchant solution is also employed for the etching steps involved in Ridge, DWG, and isolation etches.

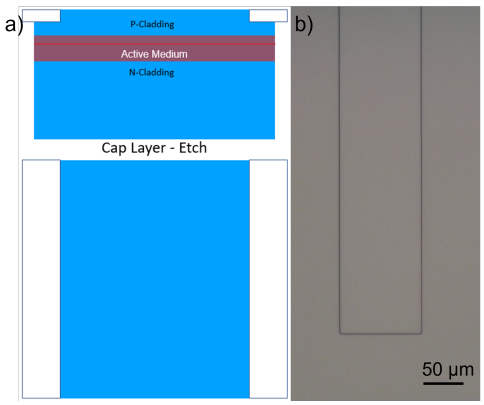

Figure 4.14: a) Cross-section and top view schematics after the cap layer etch. b) Optical microscopy image after the cap layer etch.

Ridge etch

Ridge etch is performed to create lateral optical confinement of the lasing modes. Ridge etch lines can be seen inside the cap layer previously defined in Figure 4.15. These etching lines are across multiple bars and continuous.

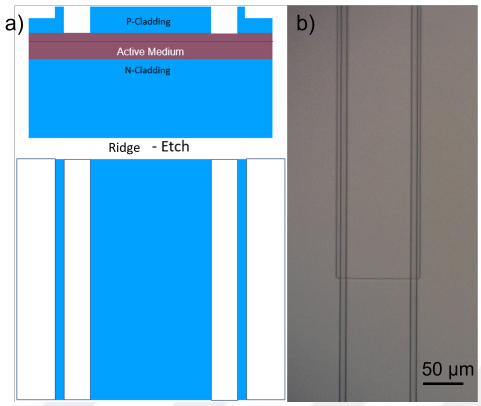

Figure 4.15: a) Cross-section and top view schematics after the ridge etch. b) Optical microscopy image after the ridge etch.

DWG etch

The DWG etching process is performed to create electrical isolation between the laser and the passive sections by etching the highly doped region to a depth that ensures both effective isolation and no optical loss. This step is of utmost importance in terms of mask alignment. The subsequent masks are aligned and defined based on markers within this layer, serving as a guide to maintain electrical isolation throughout the subsequent steps.

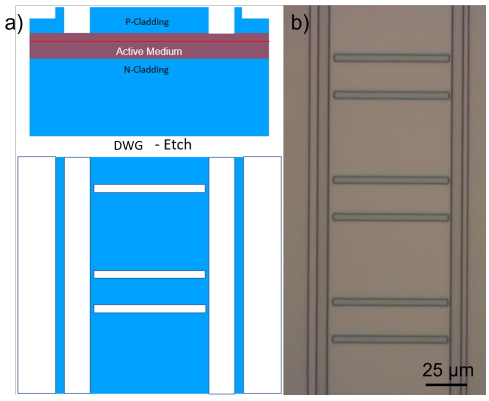

Figure 4.16: a) Cross-section and top view schematics after the DWG etch. b) Optical microscopy image after the DWG etch.

P-metal opening

We utilize silicon nitride (Si_3N_4) deposited through PECVD (Plasma-Enhanced Chemical Vapor Deposition) as the electrical isolation layer to provide current injection into the waveguide region. Subsequently, we employ a BOE (Buffered Oxide Etchant) etchant to selectively remove the dielectric layer and expose the waveguide, as illustrated in Figure 4.17. There are unpumped regions near both of the facets for improved reliability [12].

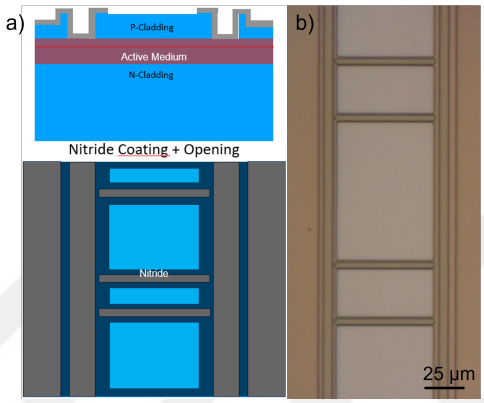

Figure 4.17: a) Cross-section and top view schematics after the P-metal opening. b) Optical microscopy image after the Si_3N_4 deposition and the P-metal opening.

P-metal deposition and lift off

First, a photoresist that has undergone a reversal bake process is applied in preparation for the lift-off procedure. Then Ti/Pt/Au with a thickness of 25nm/20nm/120nm is deposited using e-beam deposition. In Figure 4.18 b), the surface of the sample is depicted after the deposition, followed by the lift-off process. In Figure 4.18 c), the mask design is visible, wherein the lift-off stripes are continuous to maintain electrical conductivity on the mask, which will be further discussed in plating section.

Electro-plating

With the continuous electrical conductivity through the sample, we deposited 3 µm of extra gold via electroplating, resulting in improved contact resistance and uniform current injection. We should note that there is no plating near the facets where the unpumped region is present. This prevents the metal short-circuit after cleaving, increasing cleaving quality.

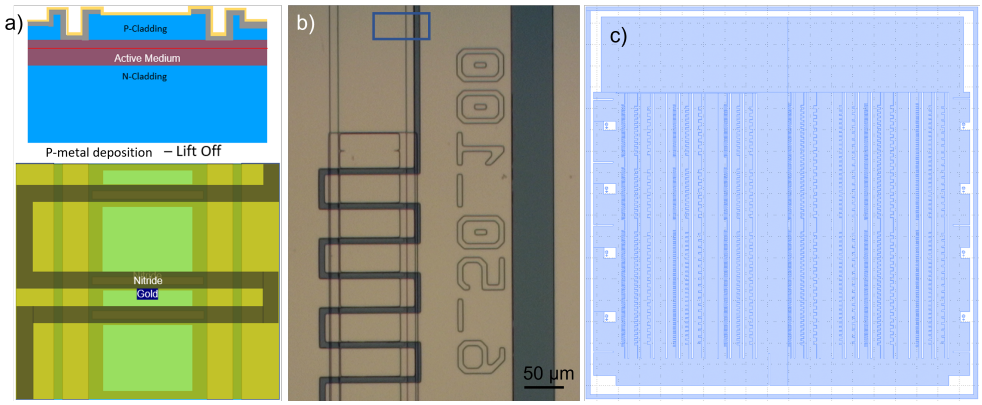

Figure 4.18: a) Cross-section and top view schematics after the metallization - lift-off. b) Optical microscopy image after the metallization - lift-off. c) Mask drawing for the lift-off step

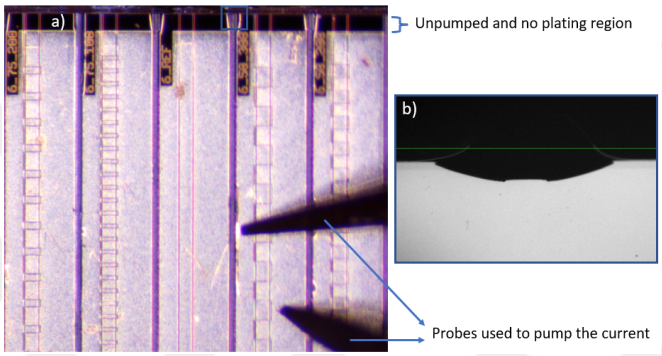

Figure 4.19: a) Top view of the cleaved sample showing unpumped and no plating region near laser output facet. b) the isolation etch image taken with TR setup camera.

Isolation and cleaving etch

During this step, the electrical isolation ridges between the LDs and the cleaving marks indicated in Figure 4.13 is etched. In our structure, the substrate is approximately 5µm from the top surface and etching around 2 µm between the LDs is enough to provide electrical isolation. However, we do 10 µm etching to provide cleaving marks.

N-metal deposition

N-side is deposited with Ge/Au with a thickness of 20nm/100nm using e-beam deposition. This process is followed by rapid thermal annealing (RTA) to allow Ge to diffuse into the substrate and to create a highly doped contact layer to reduce contact resistance.

Cleaving

Cleaving from the indicated regions in Figure 4.13 allows us to separate the laser bars. After cleaving, each facet is checked under the microscope to ensure facet cleaning and quality. Figure 4.19 (a) shows the final device with the two probes for separate current injection on the DWG-LDs. Figure 4.19 (b) shows the optical image taken with the TR setup showing the isolation etch between LDs.

4.2.3 Characterization

Our characterizations have been performed on the setup described in chapter 2, Figure 2.2. First, resistances between LDs were measured by probing two sides of isolation etchs as shown in Figure 4.20, then measuring the current with varying voltage from -3V to 3V. The current values probed were in order of 10^{-8} A, which corresponds to resistance values on the order of MΩ. This demonstrates the isolation of different emitters on the wafer as intended by the deep isolation etch step.

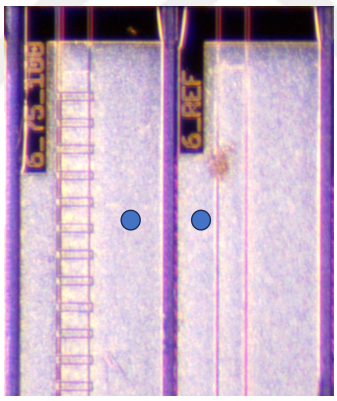

Figure 4.20: Image showing probing locations for measuring resistances between LDs.

Next, we measure the resistances between separate sections by probing laser (red) and passive (blue) sections as indicated in Figure 4.21. Our findings reveal a clear linear relationship between the resistance values and the total area dividing the sections along the cavity. For example, a 3 mm DWG-LD with a unit length of 300 µm, which exhibited a resistance of approximately 8 Ω. In comparison, an LD with the same cavity length and a section length of 100 µm had a resistance of approximately 3 Ω, with the number of sections being three times less. This relationship also holds when considering the cavity length with the same unit lengths; 3 mm LDs have resistance values approximately two times higher than those of 6 mm LDs.

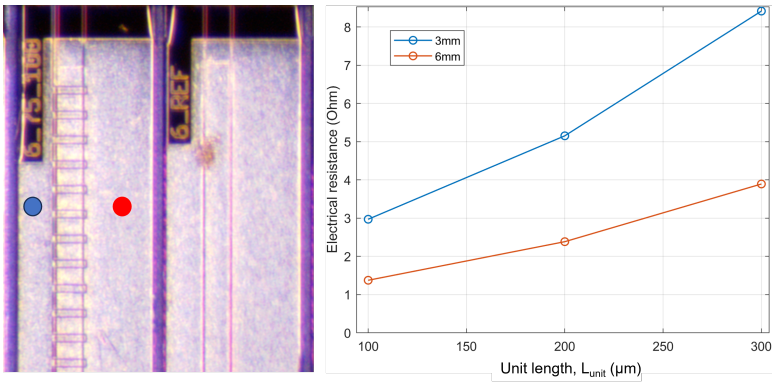

Figure 4.21: a) Image showing probing locations for measuring resistances between active and passive sections in DWG-LDs. b) Electrical resistances for section lengths of 100, 200 and 300μm for 3mm and 6mm DWG-LDs.

The resistance values indicate some leakage between the laser and passive waveguide sections. This leakage will result in changing the optimum operation power in terms of I_{pas} amount, where the higher leakage values will result in lower I_{pas} values in operation.

4.2.3.1 Light, Current and Wavelength

Based on the analysis of our simulations and the electrical resistance values between sections, we have decided to conduct initial characterizations on three main laser diodes (LDs) in order to investigate the DWG-LD devices. First, a DWG-LD with 6 mm cavity length, fill factor of %50 and laser section length of 150 μm. Although the L_{las}=150 μm exhibits relatively higher temperatures compared to shorter L_{las} LDs (see Figure 4.8 and 4.9), its electrical resistances between sections is superior to that of shorter L_{las} LDs. The second device is a 3 mm Std. LD to compare the results in the same laser heat-load density. Finally, we investigate a Std. LD with a cavity length of 6 mm to observe the effect of the same cavity length.

The setup shown in Figure 2.2 enables us to measure the power and spectrum at the same time. To ensure accurate spectral measurements, we maintain a constant temperature for each data point. This is achieved by utilizing a TEC and placing a thermocouple on the back side of the LDs to monitor the real-time temperature. The thermocouple is positioned approximately 400 μm away from the tested LD.

To maximize the heating effect, we conduct the measurements using continuous wave

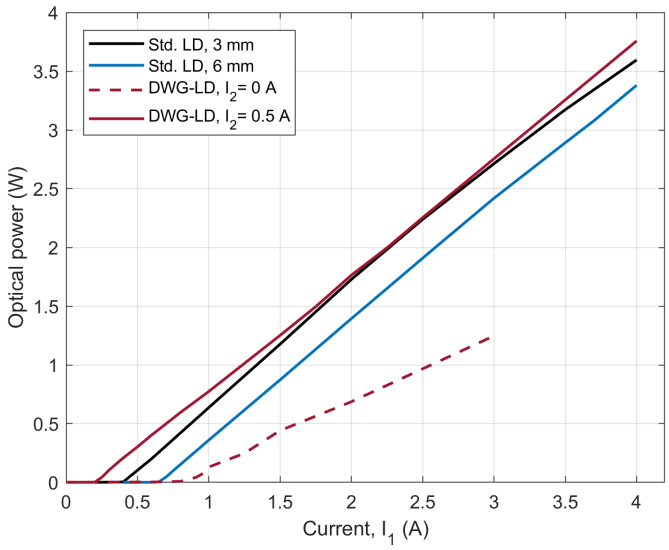

Figure 4.22: LI curves for 3 mm and 6 mm Std. LDs compared with the DWG-LD with I_{pas}= 0 A and 0.5 A.

(CW) current sources. This allows us to show the effect of DWG-LDs in the application conditions. Additionally, we set a current limit of 4 A during the measurements to prevent the lasers from reaching the COD limit. This ensures the LDs remain within safe operating conditions and enables us to proceed with subsequent thermoreflectance (TR) measurements.

Optical power output results can be seen in Figure 4.22 where the x-axis is the laser section currents until 4 A denoted as I_1. It is apparent that the DWG-LD without the passive section current (I_2) have a high loss in the unpumped regions of its waveguide, leading to a high threshold current (I_{th}) and lower slope efficiency. This also proves the electrical isolation is enough to have DWG-LD operation. When the DWG-LD is pumped with I_2= 0.5A, its threshold reduces and becomes similar to 6 mm Std. LD when compared the total applied curent ($I_{tot} = I_1 + I_2$). All three LDs exhibit similar slope efficiency $\approx$ 1 W/A confirming the effective implementation of the DWG-LD concept.

Wavelengths of the peak intensities were recorded, and its shift with laser current (I_1) is plotted as shown in Figure 4.23. The slopes of Std. 3 mm and DWG-LD are comparable, but it is lower for 6 mm Std. LD. This indicates that the laser section temperature of DWG-LD is comparable to 3mm Std. LD. and both 3mm Std. LD. and the DWG-LD operate hotter than the 6mm Std. LD due to higher current densities. However, upon examining the optical spectrum for both 3 mm Std. LD and DWG-LD at P_{op}= 3 W (see inset in Figure 4.23), there is a notable broadening towards the shorter wavelength region for the DWG-LD. This shift toward shorter wavelengths indicates lower

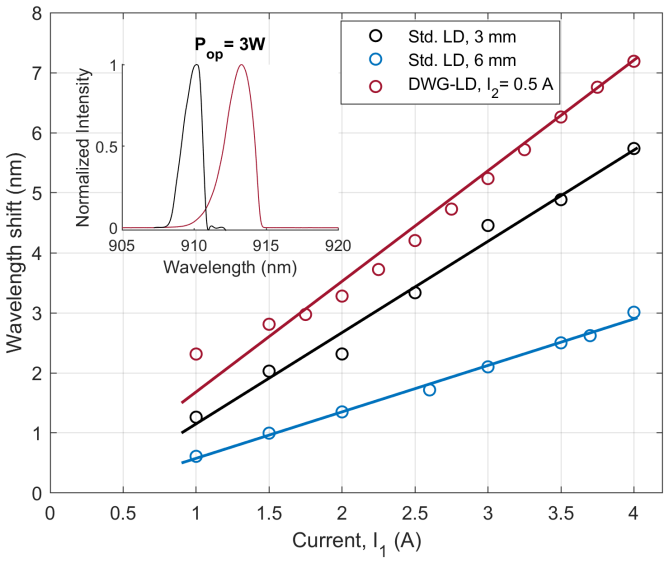

Figure 4.23: Wavelength shift data in the steady-state regime for 3 mm and 6 mm Std. LDs and the DWG-LD with I_{pas}= 0.5 A. The inset figure shows the normalized spectrum data at 3 W optical power output (P_{op}) for 3 mm Std. LD and the DWG-LD.

temperature operation in DWG-LD. This emission in a shorter wavelength region is expected in the regions between the edge of the laser sections and the neighbouring passive sections.

4.2.3.2 Facet Temperature

To have a direct measure of the temperatures in LDs, we performed thermoreflectance measurements on those LDs. To maintain consistent heating near the facets due to optical power absorption, the measurements were conducted at the same optical power output. Assuming that the LD facets are identical and have the same optical power absorption, equation Equation 2.2 indicates that the relative facet temperatures are proportional to the laser temperatures ($T_{fac} \propto T_{las}$) with a constant ΔT_{fac}.

In Figure 4.24, the facet temperature maps of all three LDs are displayed using a single color scale shown on the right-hand side. The peak facet temperatures (T_{peak}) are 74, 60, and 52 °C for Std. LD 3mm, DWG-LD, and Std. LD 6mm, respectively. The DWG-LDs demonstrated a significant reduction in the average temperature inside the cavity compared to the standard LDs, which is reflected as the reduction of the facet temperature. This indicates the effectiveness of the design changes in improving the thermal management our DWG-LDs show promising advancements in addressing thermal issues, potentially leading to improved reliability and longer lifespans for laser devices.

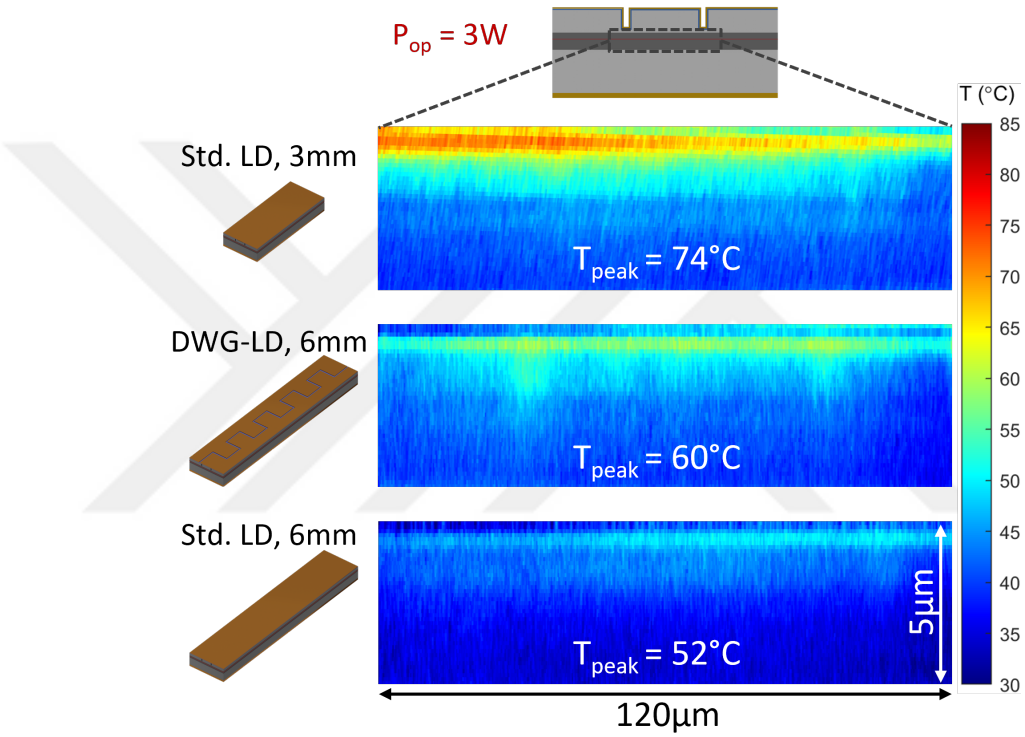

Figure 4.24: Facet temperature maps taken with TR spectroscopy. The top image illustrates the characterized region and the illustrations on the left-hand side show LDs representative models. A mutual color scale is given on the right. Peak facet temperatures (T_{peak}) can be seen temperature map.

Chapter 5

Conclusion and Discussion

Initially, we developed a 3D temperature-matching heat-transfer simulation model, which incorporates two basic boundary conditions: convective heat transfer (H) and facet absorption. These conditions were utilized to accurately replicate the experimental laser temperature (T_{las}) and the facet temperature (T_{fac}). This model allows us to analyze the heat-dissipation capabilities by generating a 3D heat-flux map and quantifying the facet absorption fraction. The facet absorption fraction serves as a valuable metric to comprehend degradation due to the increase in facet absorption, enabling benchmarking of devices concerning one another.

Using the simulation model, we have characterized two initial LDs with the same configuration and different waveguide widths. Results showed much lower temperatures for narrower waveguide width LD, even at much higher heat-load densities. We also performed high current testing and failure analysis on LDs with varying waveguide widths, ranging from narrow to broad. The results consistently supported our initial findings, revealing superior reliability in LDs with narrow waveguides despite having exponentially higher heat-load densities. To gain further insight, we analyzed the heat-flux maps generated by our simulations. We discovered that the lateral heat-flux ratio was increasing dramatically for the narrower waveguide LDs (W <50 μm) and resulting in superior heat dissipation capabilities.

To overcome the common failure mechanisms and increase the LDs' reliability, we implemented two designs utilizing electrically isolated sections. In the first design, our focus was on the primary failure mode of LDs. We conducted experiments to validate the operation of high-power edge-emitting LDs without catastrophic optical mirror

damage (COMD). To achieve this, we employed a two-section waveguide design that included a window section near the output facet, effectively isolating the facet from the high heat load of the laser. By doing so, we successfully mitigated the laser self-heating effect on the temperature-sensitive output facet. As a result, we achieved high-power operation while significantly reducing facet temperatures, eliminating the risk of COMD failure.

In the second design, we incorporated many passive sections along the waveguide. Distributed waveguide laser (DWG-LD) design aims for efficient heat dissipation of the waveguide, effectively reducing the laser temperature and subsequently lowering the facet temperatures. By implementing these passive sections, we aim to enhance the overall performance and reliability of the LD. The analysis of the LD characteristics reveals that the laser region temperatures are comparable to those of a standard LD when examining the wavelength shift. However, a closer examination of the spectrum curves and thermoreflectance results indicates that the heat distribution is visibly more effective. In particular, there is a noticeable reduction in the mean temperatures along the waveguide, suggesting an improved temperature characteristic in place.

The simulation results indicate that the effectiveness of the DWG-LD design improves when the laser section lengths (L_{las}) are kept relatively short (5 µm). However, it is important to note that as the L_{las} decreases, the electrical isolation between sections and the active current injection area also decreases significantly. To address this challenge and achieve an optimized design, it is crucial to find a solution for the electrical isolation problem.

One potential solution involves the utilization of narrow ion implantation at the DWG-etch regions. By implementing this technique, the electrical isolation problem can be effectively resolved. Consequently, it becomes feasible to design LDs with even shorter laser section lengths, resulting in significant temperature reduction and improved performance and reliability.

Bibliography

[1] Y. Liu, K. Ebadi, A. K. Sunnetcioglu, S. Gundogdu, S. Sengul, Y. Zhao, Y. Lan, Y. Zhao, G. Yang, and A. Demir, "Elimination of catastrophic optical mirror damage in continuous-wave high-power laser diodes using multi-section waveguides," *Optics Express, Vol. 30, Issue 18, pp. 31539-31549*, vol. 30, pp. 31539–31549, 8 2022.

[2] P. Crump, J. Wang, T. Crum, S. Das, M. DeVito, W. Dong, J. Farmer, Y. Feng, M. Grimshaw, D. Wise, and S. Zhang, "> 360 w and > 70% efficient GaAs-based diode lasers," *High-Power Diode Laser Technology and Applications III*, vol. 5711, p. 21, 3 2005.

[3] Y. Zhao, Z. Wang, A. Demir, G. Yang, S. Ma, B. Xu, C. Sun, B. Li, and B. Qiu, "High efficiency 1.9 kw single diode laser bar epitaxially stacked with a tunnel junction," *IEEE Photonics Journal*, vol. 13, 6 2021.

[4] Y. Lan, G. Yang, Y. Liu, Y. Zhao, Z. Wang, T. Li, and A. Demir, "808 nm broad-area laser diodes designed for high efficiency at high-temperature operation," *Semiconductor Science and Technology*, vol. 36, p. 105012, 9 2021.

[5] L. Wang, H. Qu, A. Qi, X. Zhou, and W. Zheng, "High-power laser diode at 9xx nm with 81.10% efficiency," *Optics Letters*, vol. 47, pp. 3231–3234, 7 2022.

[6] B. Saleh and M. Teich, *Fundamentals of Photonics*, ch. 14, pp. 494–541. John Wiley & Sons, Ltd, 1991.

[7] J. W. Tomm, M. Ziegler, M. Hempel, and T. Elsaesser, "Mechanisms and fast kinetics of the catastrophic optical damage (cod) in gaas-based diode lasers," *Laser and Photonics Reviews*, vol. 5, pp. 422–441, 5 2011.

[8] M. Ziegler, V. Talalaev, J. W. Tomm, T. Elsaesser, P. Ressel, B. Sumpf, and G. Erbert, "Surface recombination and facet heating in high-power diode lasers," *Applied Physics Letters*, vol. 92, p. 203506, 5 2008.

[9] M. Ziegler, M. Hempel, H. E. Larsen, J. W. Tomm, P. E. Andersen, S. Clausen, S. N. Elliott, and T. Elsaesser, "Physical limits of semiconductor laser operation: A time-resolved analysis of catastrophic optical damage," *Applied Physics Letters*, vol. 97, p. 021110, 7 2010.

[10] J. Souto, J. L. Pura, A. Torres, J. Jiménez, M. Bettiati, and F. J. Laruelle, "Catastrophic optical damage of high power ingaas/algaas laser diodes," *Microelectronics Reliability*, vol. 64, pp. 627–630, 9 2016.

[11] F. Rinner, J. Rogg, and M. T. Kelemen, "Facet temperature reduction by a current blocking layer at the front facets of high-power ingaas/algaas lasers," *Journal of Applied Physics*, vol. 93, p. 1848, 2003.

[12] J. Michaud, P. D. Vecchio, L. Bechou, D. Veyrie, M. A. Bettiati, F. Laruelle, and S. Grauby, "Precise facet temperature distribution of high- power laser diodes: Unpumped window effect," *IEEE Photonics Technology Letters*, vol. 27, pp. 1002–1005, 5 2015.

[13] L. W. Tu, E. F. Schubert, M. Hong, and G. J. Zydzik, "In-vacuum cleaving and coating of semiconductor laser facets using thin silicon and a dielectric," *Journal of Applied Physics*, vol. 80, p. 6448, 6 1998.

[14] P. Ressel, G. Erbert, U. Zeimer, K. Häusler, G. Beister, B. Sumpf, A. Klehr, and G. Tränkle, "Novel passivation process for the mirror facets of al-free active-region high-power semiconductor diode lasers," *IEEE Photonics Technology Letters*, vol. 17, pp. 962–964, 5 2005.

[15] Y. Lan, G. Yang, Y. Zhao, Y. Liu, and A. Demir, "Facet passivation process of high-power laser diodes by plasma cleaning and zno film," *Applied Surface Science*, vol. 596, p. 153506, 9 2022.

[16] R. M. Lammert, J. E. Ungar, M. L. Osowski, H. Qi, M. A. Newkirk, and N. B. Chaim, "980-nm master oscillator power amplifiers with nonabsorbing mirrors," *IEEE Photonics Technology Letters*, vol. 11, pp. 1099–1101, 9 1999.

[17] Q. Zhang, Y. Xiong, H. An, K. Boucke, and G. Treusch, "Unveiling laser diode "fossil" and the dynamic analysis for heliotropic growth of catastrophic optical damage in high power laser diodes," *Scientific reports*, vol. 6, 1 2016.

[18] P. G. Piva, S. Fafard, M. Dion, M. Buchanan, S. Charbonneau, R. D. Goldberg, and I. V. Mitchell, "Reduction of ingaas/gaas laser facet temperatures by band

gap shifted extended cavities," *Applied Physics Letters*, vol. 70, pp. 1662–1664, Mar 1997.

[19] P. W. Epperlein, "Semiconductor laser engineering, reliability and diagnostics: A practical approach to high power and single mode devices," *Semiconductor Laser Engineering, Reliability and Diagnostics: A Practical Approach to High Power and Single Mode Devices*, 1 2013.

[20] H. Naito, T. Nagakura, K. Torii, M. Takauji, H. Aoshima, T. Morita, J. Maeda, and H. Yoshida, "Long-term reliability of 915-nm broad-area laser diodes under 20-w cw operation," *IEEE Photonics Technology Letters*, vol. 27, pp. 1660–1662, 8 2015.

[21] S. Arslan, A. Demir, S. Şahin, and A. Aydinli, "Conservation of quantum efficiency in quantum well intermixing by stress engineering with dielectric bilayers," *Semiconductor Science and Technology*, vol. 33, p. 025001, 1 2018.

[22] S. Arslan, S. Gundogdu, A. Demir, and A. Aydinli, "Facet cooling in high-power ingaas/algaas lasers," *IEEE Photonics Technology Letters*, vol. 31, pp. 94–97, 1 2019.

[23] A. Demir, S. Arslan, S. Gündogdu, and A. Aydinli, "Reduced facet temperature in semiconductor lasers using electrically pumped windows," *SPIE-High-Power Diode Laser Technology XVII*, p. 24, 2019.

[24] K. Ebadi, Y. Liu, A. K. Sünnetçioglu, S. Gündogdu, S. Şengül, Y. Zhao, Y. Lan, G. Yang, and A. Demir, "Multisection waveguide method for facet temperature reduction and improved reliability of high-power laser diodes," *https://doi.org/10.1117/12.2621651*, vol. 12141, pp. 12–20, 5 2022.

[25] P. W. Epperlein, *Basic Reliability Engineering Concepts*. John Wiley & Sons, Ltd, 2013.

[26] E. Zucker, D. Zou, L. Zavala, H. Yu, P. Yalamanchili, al Erik Zucker, L. Xu, H. Xu, D. Venables, J. Skidmore, V. Rossin, R. Raju, M. Peters, K.-H. Liao, K.-W. Lee, B. Kharlamov, A. Hsieh, R. Gurram, J. Guo, N. Guerin, J. Gregg, R. Duesterberg, J. Du, A. Demir, P. Cheng, J. Cheng, H. Ishiguro, R. Li, Y. Mizoguchi, and H. Sako, "Advancements in laser diode chip and packaging technologies for application in kw-class fiber laser pumping," *https://doi.org/10.1117/12.2038268*, vol. 8965, pp. 38–51, 3 2014.

[27] Y. Sin, S. Stuart, S. LaLumondiere, M. Brodie, Z. L. Y. Sin, and Z. Lingley, "Physics of failure based reliability model of high-power ingaas-algaas strained qw lasers," *https://doi.org/10.1117/12.2507055*, vol. 10900, pp. 125–137, 3 2019.

[28] V. Spagnolo, M. Troccoli, G. Scamarcio, C. Gmachl, F. Capasso, A. Tredicucci, A. M. Sergent, A. L. Hutchinson, D. L. Sivco, and A. Y. Cho, "Temperature profile of gainas/alinas/inp quantum cascade-laser facets measured by microprobe photoluminescence," *Applied Physics Letters*, vol. 78, p. 2095, 4 2001.

[29] R. Puchert, J. W. Tomm, A. Jaeger, A. Bärwolff, J. Luft, and W. Späth, "Emitter failure and thermal facet load in high-power laser diode arrays," *Applied Physics A 1998 66:5*, vol. 66, pp. 483–486, 1998.

[30] B. J. Pandey, K. Clark, F. Abbas, E. Fuchs, K. Lascola, Y. Dikmelik, D. Hinojos, K. Hodges, D. Robbins, M. Platkov, A. Katzir, A. Suliman, G. Spingarn, A. Niguès, J.-F. Veyan, Q. Gu, and K. Roodenko, "Ir-snom on a fork: infrared scanning near-field optical microscopy for thermal profiling of quantum cascade lasers," *SPIE-Intl Soc Optical Eng*, p. 64, 1 2020.

[31] T. B. Daunis, F. Abbas, K. P. Clark, E. Fuchs, K. Lascola, Y. Dikmelik, K. Hodges, D. I. Robbins, M. Platkov, A. Katzir, Q. Gu, and K. Roodenko, "Infrared scanning near-field optical microscopy (ir-snom) for thermal profiling of quantum cascade lasers," *SPIE-Intl Soc Optical Eng*, p. 30, 3 2021.

[32] P. W. G. Epperlein, "Micro-temperature measurements on semiconductor laser mirrors by reflectance modulation: A newly developed technique for laser characterization," *Japanese Journal of Applied Physics*, vol. 32, pp. 5514–5522, 12 1993.

[33] D. Lüerßen, R. J. Ram, and J. A. Hudgings, "2-d thermal imaging of the optical power distribution in photonic integrated circuits," *Conference Proceedings - Lasers and Electro-Optics Society Annual Meeting-LEOS*, vol. 1, pp. 163–164, 2004.

[34] M. Farzaneh, K. Maize, D. Lüeren, J. A. Summers, P. M. Mayer, P. E. Raad, K. P. Pipe, A. Shakouri, R. J. Ram, and J. A. Hudgings, "Ccd-based thermoreflectance microscopy: principles and applications," *Journal of Physics D: Applied Physics*, vol. 42, p. 143001, 6 2009.

[35] B. Vermeersch, J. Christofferson, K. Maize, A. Shakouri, and G. D. Mey, "Time and frequency domain ccd-based thermoreflectance techniques for high-resolution transient thermal imaging," *Annual IEEE Semiconductor Thermal Measurement and Management Symposium*, pp. 228–234, 2010.

[36] D. Pierścińska, K. Pierściński, M. Morawiec, P. Karbownik, P. Gutowski, and M. Bugajski, "Ccd thermoreflectance spectroscopy as a tool for thermal characterization of quantum cascade lasers," *Semiconductor Science and Technology*, vol. 31, 2016.

[37] D. Pierścińska, "Thermoreflectance spectroscopy—analysis of thermal processes in semiconductor lasers," *Journal of Physics D: Applied Physics*, vol. 51, p. 013001, 11 2017.

[38] F. Duan, K. Chen, S. Wang, L. Wei, Y. Yu, and D. Ban, "Temperature profile and transient response of thermally tunable ridge waveguides with laterally supported suspension," *Applied Physics Letters*, vol. 116, p. 011102, 1 2020.

[39] K. Ebadi, *Elimination of catastrophic optical mirror damage in high-power laser diodes using multi-section waveguides*. Bilkent University, 9 2022.

[40] A. K. Jha, C. Li, K. P. Pipe, M. T. Crowley, D. B. Fullager, J. D. Helmrich, P. Thiagarajan, R. J. Deri, E. Feigenbaum, R. B. Swertfeger, and P. O. Leisher, "Thermoreflectance imaging of back-irradiance heating in high power diode lasers at several operating wavelengths," *IEEE Journal of Selected Topics in Quantum Electronics*, vol. 25, 11 2019.

[41] Y. Cong, H. Lei, H. Fa-Hong, and G. Ma-Li, "Thermal performance of laser diode array under constant convective heat transfer boundary condition," *Chinese Physics Letters*, vol. 24, pp. 1934–1937, 7 2007.

[42] C.-E. Zah, D.-H. Wu, and X. Liu, "Three-dimensional thermal model of a high-power diode laser bar," *Applied Optics, Vol. 57, Issue 33, pp. 9868-9876*, vol. 57, pp. 9868–9876, 11 2018.

[43] D.-H. Wu, C.-E. Zah, and X. Liu, "Three-dimensional thermal model of high-power semiconductor lasers," *Applied Optics*, vol. 58, p. 3892, 2019.

[44] M. Szymański, A. Kozlowska, A. Maląg, and P. Hoser, "Two-dimensional model of heat flow in edge-emitting laser revisited: A new and more versatile approach," *International Journal of Numerical Modelling: Electronic Networks, Devices and Fields*, vol. 33, p. e2745, 9 2020.

[45] M. Szymański, A. Kozłowska, J. Tomm, R. Huk, A. Maląg, and M. Rusek, "From two- to three-dimensional model of heat flow in edge-emitting laser: Theory, experiment and numerical tools," *Energies 2021, Vol. 14, Page 7006*, vol. 14, p. 7006, 10 2021.

[46] B. R. Herrero, G. Batko, J. Arias, L. Borruel, I. Esquivias, and R. Gomez-Alcala, "Modeling of facet heating in high-power laser diodes," *https://doi.org/10.1117/12.380947*, vol. 3889, pp. 96–106, 4 2000.

[47] A. K. Jha, P. O. Leisher, C. Li, K. P. Pipe, M. T. Crowley, D. B. Fullager, J. D. Helmrich, P. Thiagarajan, R. J. Deri, and R. B. Swertfeger, "Thermoreflectance-based measurement of facet optical absorption in high power diode lasers," *IEEE Photonics Technology Letters*, vol. 31, pp. 1909–1912, 12 2019.

[48] D. Hathaway, M. Shahzad, T. S. Sakthivel, M. Suttinger, R. Go, E. Sanchez, S. Seal, H. Shu, and A. Lyakh, "Output facet heating mechanism for uncoated high power long wave infrared quantum cascade lasers," *AIP Advances*, vol. 10, p. 85104, 2020.

[49] R. McKenna, S. Corbett, S. T. Naimi, D. Mickus, D. McCloskey, and J. F. Donegan, "Thermoreflectance imaging of semiconductor lasers with a numerical thermal model," *IEEE Journal of Selected Topics in Quantum Electronics*, vol. 28, 1 2022.

[50] Y. Liu, G. Yang, Z. Wang, T. Li, S. Tang, Y. Zhao, Y. Lan, and A. Demir, "High-power operation and lateral divergence angle reduction of broad-area laser diodes at 976 nm," *Optics and Laser Technology*, vol. 141, p. 107145, 2021.

[51] A. Demir, K. Ebadi, Y. Liu, A. K. Sünnetçioğlu, S. Gündoğdu, S. Şengül, Y. Zhao, Y. Lan, and G. Yang, "COMD-free continuous-wave high-power laser diodes by using a multi-section waveguide method," *https://doi.org/10.1117/12.2650619*, vol. 12403, pp. 86–93, 3 2023.

[52] A. Demir, M. Peters, R. Duesterberg, V. Rossin, and E. Zucker, "Semiconductor laser power enhancement by control of gain and power profiles," *IEEE Photonics Technology Letters*, vol. 27, p. 2178–2181, 2015.

[53] Y. Liu, G. Yang, Y. Zhao, S. Tang, Y. Lan, Y. Zhao, and A. Demir, "48 w continuous-wave output from a high- efficiency single emitter laser diode at 915 nm," *IEEE Photonics Technology Letters*, vol. 34, pp. 1218–1221, 11 2022.